








The C-Band All-Sky Survey (C-BASS): template fitting of diffuse galactic microwave emission in the northern sky

S. E. Harper ¹★, C. Dickinson ^{1,2}, A. Barr,¹ R. Cepeda-Arroita ¹, R. D. P. Grumitt ³,
H. M. Heilgendorff,⁴ L. Jew,³ J. L. Jonas,^{5,6} M. E. Jones ³, J. P. Leahy,¹ J. Leech,³ T. J. Pearson ²,
M. W. Peel ^{7,8}, A. C. S. Readhead² and A. C. Taylor³

¹Jodrell Bank Centre for Astrophysics, Alan Turing Building, Department of Physics & Astronomy, School of Natural Sciences, The University of Manchester, Oxford Road, Manchester M13 9PL, UK

²Cahill Centre for Astronomy and Astrophysics, California Institute of Technology, Pasadena, CA 91125, USA

³Sub-department of Astrophysics, University of Oxford, Denys Wilkinson Building, Keble Road, Oxford OX1 3RH, UK

⁴School of Mathematics, Statistics & Computer Science, University of KwaZulu-Natal, Westville Campus, Private Bag X54001, Durban, South Africa

⁵Department of Physics and Electronics, Rhodes University, Grahamstown 6139, South Africa

⁶South African Radio Astronomy Observatory, 2 Fir Road, Observatory, Cape Town 7925, South Africa

⁷Instituto de Astrofísica de Canarias, E-38205 La Laguna, Tenerife, Spain

⁸Departamento de Astrofísica, Universidad de La Laguna (ULL), E-38206 La Laguna, Tenerife, Spain

Accepted 2022 April 25. Received 2022 April 25; in original form 2022 February 25

ABSTRACT

The C-Band All-Sky Survey (C-BASS) has observed the Galaxy at 4.76 GHz with an angular resolution of 0°73 full-width half-maximum, and detected Galactic synchrotron emission with high signal-to-noise ratio over the entire northern sky ($\delta > -15^\circ$). We present the results of a spatial correlation analysis of Galactic foregrounds at mid-to-high ($b > 10^\circ$) Galactic latitudes using a preliminary version of the C-BASS intensity map. We jointly fit for synchrotron, dust, and free-free components between 20 and 1000 GHz and look for differences in the Galactic synchrotron spectrum, and the emissivity of anomalous microwave emission (AME) when using either the C-BASS map or the 408-MHz all-sky map to trace synchrotron emission. We find marginal evidence for a steepening ($\langle \Delta\beta \rangle = -0.06 \pm 0.02$) of the Galactic synchrotron spectrum at high frequencies resulting in a mean spectral index of $\langle \beta \rangle = -3.10 \pm 0.02$ over 4.76–22.8 GHz. Further, we find that the synchrotron emission can be well modelled by a single power law up to a few tens of GHz. Due to this, we find that the AME emissivity is not sensitive to changing the synchrotron tracer from the 408-MHz map to the 4.76-GHz map. We interpret this as strong evidence for the origin of AME being spinning dust emission.

Key words: radiation mechanisms: non-thermal – radiation mechanisms: thermal – surveys – cosmology: diffuse radiation – radio continuum: ISM.

1 INTRODUCTION

Large-scale diffuse Galactic radio emission, at frequencies 0.1–50 GHz, is composed of three principal components: synchrotron emission from the propagation of cosmic rays through the Galactic magnetic field (e.g. Strong, Orlando & Jaffe 2011), thermal free-free emission from ionized gas (e.g. Dickinson, Davies & Davis 2003), and spinning dust emission from the rapid rotation of small grains in the interstellar medium (ISM) (e.g. Dickinson et al. 2018). The study of these Galactic components is important both for understanding the astrophysics of our Galaxy, and also for studies of the cosmic microwave background (CMB) (e.g. de Oliveira-Costa et al. 2008; Bonaldi & Ricciardi 2011; Remazeilles et al. 2016).

There are only a limited number of radio surveys that preserve the large-scale structure of Galactic emission. The all-sky 408-MHz map (Haslam et al. 1982) has become the standard map for tracing

Galactic synchrotron emission as it has little impact from both synchrotron self-absorption and free-free contamination. However, the 408-MHz map is limited by being total intensity only and having numerous systematics that are challenging to quantify (Remazeilles et al. 2015). Other radio surveys of the large-scale Galactic structure at 820 MHz (Berkhuijsen 1972), 1420 MHz (Reich, Testori & Reich 2001; Calabretta, Staveley-Smith & Barnes 2014), and 2.3 GHz (Reif et al. 1987; Jonas, Baart & Nicolson 1998) are also limited due either to partial sky coverage, systematics, and being in total intensity only ($I + Q$ for the 2.3-GHz map). The S-band Polarization All-Sky Survey (S-PASS; Carretti et al. 2019) provided the first map of polarized emission in the Southern sky using the Parkes telescope at 2.3 GHz. New data from the Q-U-I JOint Tenerife (QUIJOTE) experiment at 10–20 GHz will complement these surveys in the Northern hemisphere (Génova-Santos et al. 2015; Guidi & Quijote Collaboration 2020).

The limited number of surveys at the intermediate frequencies between 408 MHz and the lowest frequency Wilkinson Microwave Anisotropy Probe (WMAP) 22.8-GHz band means that capturing

* E-mail: stuart.harper@manchester.ac.uk

spectral curvature in the synchrotron component is almost impossible. We expect to see spectral steepening in the synchrotron emission due to energy losses in the cosmic-ray electron (CRE) population (e.g. Strong et al. 2011) or potentially even flattening due to re-energization of the CRE population from active star formation regions (Bennett et al. 2003). The ARCADE2 results suggest that there is evidence for synchrotron spectral curvature (Kogut et al. 2011); however, the ARCADE2 survey was limited to a relatively small portion of the sky.

There are also still many unknown quantities regarding dust emission at radio frequencies, commonly referred to as either anomalous microwave emission (AME) (Kogut et al. 1996; Leitch et al. 1997) or, when linked with polycyclic aromatic hydrocarbons (PAHs) or very small grains, spinning dust emission (Draine & Lazarian 1998b; Ali-Haïmoud, Hirata & Dickinson 2009). The *Planck* COMMANDER analysis has provided the current best all-sky map of AME (Planck Collaboration XII 2014; Planck Collaboration IV 2020). However, it was found that the COMMANDER analysis derived AME amplitude can differ by 30–50 per cent when compared to other analyses due to correlations with free-free and synchrotron emission components even in mid-to-high latitude ($b > 10^\circ$) regions (Planck Collaboration XXV 2016). Similarly, Cepeda-Arroita et al. (2021) found significant differences in the fitted AME amplitude when using both the C-BASS and 408-MHz data to constrain low frequencies rather than just the 408-MHz data alone in the λ -Orionis region.

The study of AME, free-free and synchrotron emission at mid-to-high latitudes can be greatly improved by using a cleaner estimate of the synchrotron emission at WMAP and *Planck* frequencies. C-BASS offers just such an estimate as it is nearer in frequency, meaning that it will be less impacted by spectral curvature. Further advantages of the C-BASS map over the 408-MHz map are a well-understood beam response, allowing the map to be deconvolved to a known Gaussian beam pattern, and well-understood noise and systematics; all of which are not available for the 408-MHz map. At present, only the northern part of the C-BASS survey is complete, but this will be extended to the full-sky in the future.

In this paper, we use a preliminary version of the C-BASS intensity map of the northern sky to perform a pixel-space template fitting correlation analysis, a method that has a long heritage for studying Galactic foregrounds (e.g. de Oliveira-Costa et al. 1997; Banday et al. 2003; Bennett et al. 2003; Davies et al. 2006; Ghosh et al. 2012; Peel et al. 2012). We use the C-BASS map in combination with the 408-MHz map to estimate the degree of spectral curvature across the sky in regions of approximately 100 deg^2 . We also investigate if there is any change in the fitted dust coefficients at 22.8 GHz when using C-BASS in place of the 408-MHz map, and look for any evidence of a hard synchrotron component that may explain some or all of the observed AME at mid-to-high latitudes (Peel et al. 2012). Finally, we look to see if there is any preference for any particular dust tracer when measuring AME at mid-to-high latitudes.

The paper is organized as follows: In Section 2, we provide an overview of the C-BASS experiment, data-reduction methods, and map-making. In Section 3, we describe all the ancillary data sets used in this analysis. In Section 4, we outline the template fitting method as well as the masks and regions that we use to divide up the sky. In Section 5, we outline the results of the template fitting analysis. In Section 6, we fit model spectra of spinning dust and thermal dust to the dust template fitting coefficients. Finally, in Section 7, we discuss the results of the template fitting analysis in a wider context before giving concluding remarks and a summary in Section 8.

2 C-BASS NORTH

In this work, we will use a preliminary version of the C-BASS intensity data. The C-BASS map presented here is identical to that used in Dickinson et al. (2019) and Cepeda-Arroita et al. (2021) except for a global calibration correction resulting in a 2.1 per cent decrease in brightness; there is also a decrease in calibration uncertainty from 5 to 3 per cent. This map will be almost identical to the final C-BASS intensity map except for small changes in data selection and processing aimed at eliminating subtle artefacts in the polarization data, which have negligible effect on the intensity maps. In the following sections, we give an overview of the C-BASS data-reduction pipeline. More details will be given in the upcoming C-BASS survey papers (Taylor et al., in preparation and Pearson et al., in preparation).

2.1 Northern survey and instrument

The C-BASS project aims to map the entire sky in intensity and polarization at 4.76 GHz (Jones et al. 2018). The northern survey used a 6.1-m dish based at the Owens Valley Radio Observatory, with a nominal full-width half-maximum (FWHM) resolution of $0'.73$. The antenna uses a Gregorian optical configuration that was designed to minimize sidelobe power by both underilluminating the primary reflector and surrounding it in a radio absorbing baffle. Furthermore, to ensure a circularly symmetric beam pattern, the support struts for the secondary reflector were removed and it was instead supported by a low-loss dielectric foam cone (Holler et al. 2013).

The C-BASS instrument is a dual circularly polarized correlation radiometer that can obtain instantaneous measurements of Stokes parameters I, Q, and U. The receiver's nominal bandpass is 4.5–5.5 GHz but notch filters were used to suppress local radio frequency interference (RFI), reducing the effective bandwidth to 0.5 GHz. Receiver stability is maintained by a continuous comparison between the sky and a resistive load that minimizes $1/f$ noise fluctuations. For details of the C-BASS receiver system, see King et al. (2014).

The C-BASS northern survey observations were taken between 2012 and 2015. The survey scanning strategy slewed the telescope at a set of fixed elevations, between $37^\circ.2$ and $77^\circ.2$, over full 360° sweeps in azimuth. The slewing rate was $\approx 4^\circ \text{ s}^{-1}$ but was varied slightly between observations to average out any possible scan-synchronous instrumental systematics from the final C-BASS map. This observing strategy maps all declinations above -15° , and covers approximately a $26\,000 \text{ deg}^2$ area of sky. A full description of the northern survey maps will be given in Taylor et al. (in preparation).

2.2 C-BASS data reduction

The C-BASS data are processed through a standard pipeline procedure, the details of which will be outlined in forthcoming papers (Pearson et al., in preparation and Taylor et al., in preparation). However, we provide a brief summary here. The key tasks of the pipeline are to flag sources of RFI and Solar system objects, calibrate the data to brightness temperature units, and remove a number of systematic effects from the data. The two main systematics that are modelled and tracked are: a microphonics signal caused by the cryocooler system, which induces a 1.2-Hz signal into the time-ordered data (TOD); and emission from the ground detected in the far sidelobes.

Relative calibration is performed by injecting a regular noise diode signal into the front-end of the receiver. The noise diode is found to be stable to the level of 1 per cent or better over many months,

resulting in a relative calibration better than 1 per cent in total. The calibration to the astronomical brightness scale is done using daily observations of Tau A and Cas A using the WMAP derived models for the flux density of these sources (Weiland et al. 2011). The bandpass-weighted central frequency of the C-BASS North intensity data is 4.76 GHz when calibrated to a flat-spectrum ($\beta = -2^1$) source. Over the realistic range of source spectral indices observed in the C-BASS map ($-3.5 < \beta < -2$), colour corrections will contribute less than a 1 per cent uncertainty. One remaining source of uncertainty is the primary beam deconvolution; tests of sources flux densities in the final C-BASS map suggest that the deconvolution (Section 2.3.2) has an additional 1 per cent uncertainty. However, at present, the C-BASS calibration is still being finalized in preparation for the public release of the survey (Taylor et al. in preparation), as such we adopt a conservative 3 per cent calibration uncertainty for this work.

2.3 C-BASS maps

2.3.1 Map making

To produce the C-BASS maps, we use the destriping map-maker *Descart* (Sutton et al. 2010). We use a destriping offset length of 5 s to remove any large-scale $1/f$ noise in the data. The C-BASS map does not include day-time data due to the impact of the Sun in the far-sidelobes of the beam on the large-scale structures in the map. The final map has a $0^{\circ}.73$ FWHM, with a sensitivity of approximately 0.25 mK/beam (instrumental white noise only). To estimate the level of the residual $1/f$ noise in the map, we performed a jack-knife test where we split the C-BASS observations into two approximately equal-sized data sets, and produced a map for each. Differencing the two maps, we compared the ratio of the root mean squared (RMS) estimated in the residual data (which contains both residual $1/f$ and white noise) to the expected RMS assuming just white noise. We find that on average the C-BASS map has a 10 per cent excess of residual $1/f$ noise at scales of a few degrees and larger, which is negligible relative to other sources of uncertainty.

2.3.2 Deconvolution

The C-BASS beam is diffraction-limited with a main beam efficiency of 72.8 per cent (i.e. the power within the first null, which is at 1°). The sidelobe structures of the C-BASS beam are imprinted into the final map and result in an effective calibration which varies with angular scale. In previous C-BASS papers (Irfan et al. 2015; Dickinson et al. 2019; Cepeda-Arroita et al. 2021), this resulted in an effective calibration uncertainty due to the beam of approximately 5 per cent.

We have accurately characterized the C-BASS beam using detailed physical optics simulations verified by observations of bright point sources and direct beam measurements using a radio transmitter, improving the measurements presented by Holler et al. (2013). This allows us to deconvolve the effect of the beam, resulting in an effective Gaussian beam and a window function that is largely flat in log-harmonic space.

The deconvolution of the C-BASS map is done in spherical harmonic space using the routines provided by *HEALPIX* (Górski et al. 2005). First, we transform the C-BASS beam model into a

spherical harmonic transfer function (B_{ℓ}). Next, we generate the transfer function for the 1° Gaussian beam that we wish to smooth to (G_{ℓ}) and divide this by the derived C-BASS beam transfer function. More details of the beam transfer function can be found in the C-BASS northern survey paper (Taylor et al. in preparation). Finally, we multiply the ratio of the transfer function with the spherical harmonic amplitudes of the map such that the deconvolved C-BASS map is

$$m(\theta, \phi) = \sum_{\ell=0}^{\infty} \sum_{m=-\ell}^{\ell} a_{\ell,m} \frac{G_{\ell}}{B_{\ell}} Y_{\ell}^m(\theta, \phi), \quad (1)$$

where $m(\theta, \phi)$ is the map along the line of sight defined by θ and ϕ , G_{ℓ} is a 1° Gaussian beam transfer function, B_{ℓ} is the C-BASS beam transfer function, and $Y_{\ell}^m(\theta, \phi)$ are spherical harmonics. We find that after beam deconvolution the calibration of the map on all angular scales is 1 per cent or better, with the remaining uncertainty due to small asymmetries in the beam.

2.3.3 Background source subtraction

After deconvolution of the map, we subtract a model of the extragalactic background point sources. At the frequency and resolution of the C-BASS data the sky is confusion-limited at the level of ≈ 0.7 mK deg $^{-1}$ (Section 4.5 for details), which is several times greater than the instrumental noise level in the map. To remove the sources, we use a combination of catalogues. We use the C-BASS-derived point source catalogue described in Grumitt et al. (2020) for all sources that are detected at 10σ or better and do not lie within $|b| < 1^{\circ}$ of the Galactic plane. For fainter sources, or sources with a poor detection using C-BASS itself, we use several C-band point source catalogues: the Green Bank 6 cm (GB6) survey (Gregory et al. 1996), the Parkes-MIT-NRAO (PMN) survey (Wright et al. 1994) (for low declinations), and the RATAN-800 survey (Mingaliev et al. 2007) for sources missed by the GB6 survey around the North Celestial Pole (NCP).

The sources' flux densities were binned in $a_{\ell m}$ space and multiplied by the beam transfer function as

$$a_{\ell m} = \sum_{i=1}^{N_s} S_i Y_{\ell}^m(\theta_i, \phi_i) B_{\ell}, \quad (2)$$

where S_i is the source flux density from one of the catalogues, N_s is the number of sources in the catalogue, B_{ℓ} is the transfer function for the deconvolved C-BASS map at 1° resolution, and Y_{ℓ}^m are spherical harmonics. We note that for some sources, specifically those near the Galactic plane or with large flux densities, this method will not result in the perfect subtraction of the source because of small pointing offsets, changes in source flux densities, or systematic errors in the measurement of the source flux density. In this analysis, we mask bright sources with $S_{4.76\text{GHz}} > 1$ Jy. Section 4.3 provides more details on masking.

3 ANCILLARY DATA

Here, we provide an overview of all the ancillary data sets. All data sets are smoothed to a common resolution of 1° FWHM, using beam transfer functions where available, i.e. for C-BASS, WMAP, and *Planck*. For WMAP and *Planck* maps, the CMB has been subtracted using the Spectral Matching Independent Component Analysis (SMICA) estimate from Planck Collaboration XII (2014). A summary of all the data sets used is given in Table 1.

¹Defined in brightness temperature units as $T_b \propto \nu^{\beta}$.

Table 1. Data sets used in this analysis. The first block of maps are used as templates for fitting the synchrotron, free–free, and dust components. The second block lists the maps to which we applied the template fitting procedure.

Telescope/survey	Frequency (GHz)	FWHM (arcmin)	σ_{cal} (%)	Reference	Notes
Haslam	0.408	51	10	Remazeilles et al. (2015)	Synchrotron template
C-BASS	4.76	44	3	This work	Synchrotron template
WHAM H α	N/A	1	10	Dickinson et al. (2003), Finkbeiner (2003)	Free–free template
<i>Planck</i> HFI 353 GHz	353	4.7	5	Planck Collaboration I (2020)	Dust template
<i>Planck</i> 353 GHz optical depth	353	5.0	5	Planck Collaboration XI (2014)	Dust template
<i>Planck</i> dust radiance \mathfrak{R}	–	5.0	–	Planck Collaboration XI (2014)	Dust template
IRAS100 μm	2997	4.3	13.5	Miville-Deschenes & Lagache (2005)	Dust template
FDS8 model 8	94	6.1	–	Schlegel, Finkbeiner & Davis (1998)	Dust template
WMAP <i>K</i> band	22.8	51.3	3	Bennett et al. (2013)	9-year
<i>Planck</i> LFI 30 GHz	28.4	33.16	3	Planck Collaboration I (2020)	PR3
WMAP <i>Ka</i> -band	33.0	39.1	3	Bennett et al. (2013)	9-year
WMAP <i>Q</i> -band	40.7	30.8	3	Bennett et al. (2013)	9-year
<i>Planck</i> LFI 44 GHz	44.1	28.09	3	Planck Collaboration I (2020)	PR3
WMAP <i>V</i> -band	60.7	30.8	3	Bennett et al. (2013)	9-year
<i>Planck</i> LFI 70 GHz	70.4	13.08	3	Planck Collaboration I (2020)	PR3
WMAP <i>W</i> -band	93.5	30.8	3	Bennett et al. (2013)	9-year
<i>Planck</i> HFI 143 GHz	143	7.18	5	Planck Collaboration I (2020)	PR3
<i>Planck</i> HFI 217 GHz	217	4.87	5	Planck Collaboration I (2020)	PR3
<i>Planck</i> HFI 353 GHz	353	4.7	5	Planck Collaboration I (2020)	PR3
<i>Planck</i> HFI 545 GHz	545	4.73	5	Planck Collaboration I (2020)	PR3
<i>Planck</i> HFI 857 GHz	857	4.51	5	Planck Collaboration I (2020)	PR3
IRAS100 μm	2997	4.3	13.5	Miville-Deschenes & Lagache (2005)	IRIS

3.1 Synchrotron templates

As well as using the C-BASS map (Section 2) to trace the diffuse synchrotron emission we also use the 408-MHz radio continuum survey by Haslam et al. (1982), which has remained for decades the best tracer of diffuse Galactic synchrotron emission at WMAP and *Planck* frequencies. The survey was undertaken during the 1960 and 1970s and combines observations from the Effelsberg 100 m, and the Jodrell Bank 76 m Mk1 and Mk1a telescopes in the Northern hemisphere, and data from the Parkes 64 m telescope for the Southern hemisphere.

The average FWHM of the original map produced by Haslam et al. (1982) is 56 arcmin. Calibration and zero level offsets were set by an earlier 404-MHz survey (Pauliny-Toth & Shakeshaft 1962). The expected calibration uncertainty is 10 per cent. However, no deconvolution of the beam is possible, therefore we do not know how the calibration changes with angular scale.

The original 408-MHz map has in recent years been improved in Remazeilles et al. (2015), which reduces striping due to instrumental systematics in the original data via Fourier filtering, and also provides an improved subtraction of point sources in the map. For this analysis, we use the destriped and desourced map provided by Remazeilles et al. (2015) from the Microwave Background Data Analysis (LAMBDA) website.²

3.2 Free–free template

The best currently available method for tracing free–free emission at mid-to-high Galactic latitudes is to use the H α ($\lambda 656.28$ nm) emission line. This is because for a given HII region the brightness at radio frequencies and the intensity of the H α transition are both dependent on just the emission measure and the electron temperature of the plasma (Draine 2011).

H α emission is particularly sensitive to dust extinction, which acts to reduce the H α intensity along any given line of sight. H α maps are also contaminated by stellar continuum emission that must be carefully subtracted. We use the all-sky composite H α maps given by Dickinson et al. (2003) and Finkbeiner (2003) as templates for the free–free emission. Both combine publicly available H α data sets but approach the correction for dust absorption and continuum removal slightly differently. The Finkbeiner (2003) data set assumes no correction for dust absorption, while for the Dickinson et al. (2003) H α maps we use two dust mixing fractions: $f_d = 0$ and 0.33.

3.3 Dust templates

We use the reprocessed IRAS 100- μm data (IRIS), which has a global calibration uncertainty of 13.5 per cent (Miville-Deschenes & Lagache 2005). The IRAS 100 μm ($I_{100\mu\text{m}}$) is primarily a tracer of cold interstellar dust, however, it is somewhat sensitive to the local interstellar radiation field (ISRF) since it is near the peak of the thermal dust emission spectrum (Tibbs et al. 2013).

To trace the cold thermal dust component on the Rayleigh–Jeans tail of the thermal dust spectrum, we use the *Planck* 353-GHz map (I_{353}) (Planck Collaboration I 2020), as well as the derived dust optical depth at 353 GHz (τ_{353}) (Planck Collaboration X 2016). These maps are directly proportional to the dust column (Planck Collaboration XI 2014) but should be insensitive to changes in the ISRF. At frequencies around the peak of the thermal dust spectrum, the τ_{353} data are a better tracer of Galactic dust emission than I_{353} since they do not contain cosmic infrared background anisotropies.

We use the *Planck*-derived dust radiance map (Planck Collaboration XI 2014), which is the integrated bolometric intensity of the dust grains. The dust radiance is proportional to the amount of light absorbed by the dust and as such is directly proportional to the ISRF as well as the dust column.

Finally, to make comparisons with previous works, we also include the 94 GHz dust brightness map derived from model 8 in Schlegel

²<http://lambda.gsfc.nasa.gov>

et al. (1998), which we will refer to as FDS8. The FDS8 map is an extrapolation of the 100 and 240- μm IRAS maps calibrated to the *COBE*-FIRAS spectral data. For many previous studies of dust correlated AME, this map has been used, however, it has been superseded by direct observations of these frequencies by the *Planck* mission.

3.4 WMAP data

We use the Wilkinson Microwave Anisotropy Probe (WMAP) 9-year data release (Bennett et al. 2013) convolved to a Gaussian 1° resolution beam obtained from the LAMBDA website. The WMAP satellite observations were made using ten differencing assemblies at five frequencies from 23 to 94 GHz. The original FWHM resolution of the instrument was 0.93 to 0.23 . For the calibration uncertainty of the WMAP maps, we assign a 3 per cent uncertainty to account for colour corrections and residual beam asymmetries. We convert all the maps to brightness temperature units from thermodynamic units relative to the CMB.

3.5 Planck data

We use the 2018 release of the *Planck* all-sky maps (Planck Collaboration I 2020). The *Planck* low-frequency instrument (LFI) was a pseudo-correlation radiometer that operated between 30 and 70 GHz, with FWHM resolutions of 33 to 13 arcmin; and the high-frequency instrument (HFI) used bolometers that spanned a frequency range of 100–857 GHz, with resolutions of 7.2–4.5 arcmin FWHM. We adopt calibration uncertainties for the LFI of 3 per cent (Planck Collaboration Int. XV 2014) and HFI of 5 per cent (Planck Collaboration I 2020); these uncertainties account for colour corrections, residual beam asymmetries, and other systematics. Units were converted from thermodynamic units relative into the CMB to brightness temperature units.

4 TEMPLATE FITTING

4.1 Method

To estimate the contribution of a given emission component to each frequency map, we use a template fitting method (also referred to as a correlation analysis); a technique that has been well established for studying Galactic foregrounds (Kogut et al. 1996; de Oliveira-Costa et al. 1997; Davies et al. 2006; Planck Collaboration XXI 2011; Ghosh et al. 2012; Peel et al. 2012; Planck Collaboration Int. XXII 2015). The method assumes that the sky signal can be decomposed into a linear combination of N_Z template maps, where each template is chosen to trace a single emission component. Template fitting is performed by solving for the template coefficients \mathbf{a} in

$$\mathbf{d} = \mathbf{Z}\mathbf{a} + \mathbf{n}, \quad (3)$$

where each column of \mathbf{Z} ($N_{\text{pix}} \times N_Z$) contains the N_{pix} pixel intensities of the templates used to decompose the sky vector \mathbf{d} (N_{pix}). We want to solve for the template coefficients vector \mathbf{a} , where each coefficient describes the radio brightness of a given emission component at a given frequency per unit template. Least-squares solution gives

$$\hat{\mathbf{a}} = (\mathbf{Z}^T \mathbf{N}^{-1} \mathbf{Z})^{-1} \mathbf{Z}^T \mathbf{N}^{-1} \mathbf{d}, \quad (4)$$

where \mathbf{N}^{-1} is the pixel noise covariance matrix. The details of the noise covariance matrix are described in Section 4.5.

We fit for the synchrotron, dust, and free-free emission components, as well as an arbitrary offset. Before we perform the template

fit we first subtract the mean offset of each template. Subtracting an offset from each template does not impact the fitted coefficients but does improve convergence and removes arbitrary correlations between templates and the data.

Coefficient uncertainties can be calculated using the covariance of the coefficients as

$$\mathbf{C}_a = \mathbf{Z}^T \mathbf{N}^{-1} \mathbf{Z}, \quad (5)$$

where each parameter is as defined in equation (4). However, estimating the coefficient uncertainties in this manner requires both the templates to be perfect representations of the underlying emission, and for the noise to be Gaussian distributed in each data set. Therefore we instead estimate uncertainties and the correlation between coefficients using the bootstrapping method (Efron 1979; Efron & Tibshirani 1986). The bootstrapping method gives unbiased estimates of the uncertainties in the coefficients by randomly resampling with replacement the pixels in each region. Resampling is done 1000 times for each region resulting in uncertainties in the bootstrapped coefficient uncertainties of ≈ 3 per cent. We estimate the coefficient covariance matrix by averaging over the outerproduct of all the estimates of \mathbf{a} ,

$$\mathbf{C}_a = \langle \hat{\mathbf{a}} \hat{\mathbf{a}}^T \rangle. \quad (6)$$

We find that for regions far from bright sources of Galactic emission the differences between the coefficient uncertainties estimated using equations (5) and (6) were small – the bootstrapped uncertainties were 10–20 per cent larger for data between 5 and 60 GHz. However, for regions nearer to the Galactic plane, or coincident with bright features (i.e. Eridanus/Orion – regions 69, 82, 83, and 97 in Fig. 2) the bootstrapped uncertainties can be as much as an order-of-magnitude larger. For the higher frequencies ($\nu > 143$ GHz), the bootstrapped uncertainties were systematically larger in all regions by as much as an order-of-magnitude, which is likely due to not including any additional sources of noise at high frequency other than the instrument noise. Therefore, it is clear that the bootstrapped uncertainties are more reliable and representative of the data.

4.2 Free-free emission removal

The C-BASS map contains contributions from both synchrotron and free-free emission, the latter from the warm-ionized medium (WIM). When using the 4.76-GHz C-BASS map as a synchrotron template we first subtract a global estimate of the free-free emission using the $\text{H}\alpha$ data. We use the best-fitting $\text{H}\alpha$ coefficient at 4.76 GHz of $T_b^{\text{ff}}/I_{\text{H}\alpha} = (195 \pm 5) \mu\text{K/R}$ (see Section 5.3 for derivation of this value) to scale the $\text{H}\alpha$ data, and then subtract this from the C-BASS map.

It is possible that subtracting the free-free emission in the C-BASS map may result in systematic biases in later results (since we are using the same $\text{H}\alpha$ map to trace free-free emission at higher frequencies). Therefore, we subtracted free-free templates from the C-BASS data using fixed electron temperature values of 5000, 6000, 7000, and 8000 K using equation (15). Changing the amplitude of the subtracted free-free component resulted in no significant change in the fitted coefficients discussed in Section 5, which is not unexpected since free-free emission contributes less than 20 per cent of the total emission at 4.76 GHz at high Galactic latitudes.

4.3 Mask

Template fitting is only as effective as the templates that trace the underlying emission components at a given frequency. In order to

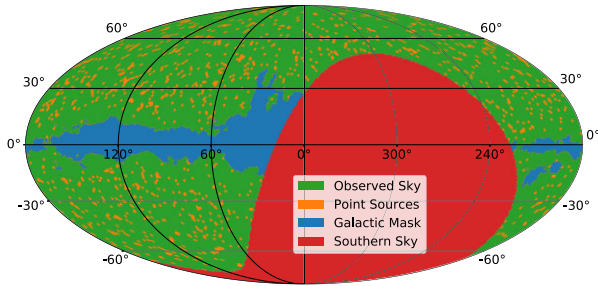


Figure 1. Sky mask used for template fitting plotted in a Galactic Mollweide projection. Only the *green* pixels are used in the template fitting analysis.

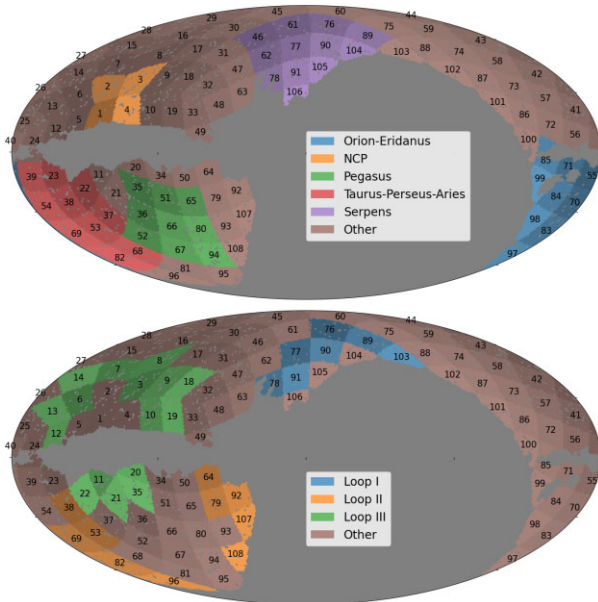


Figure 2. Mollweide projection in Galactic coordinates of the 108 $N_{\text{side}} = 4$ regions used to sub-divide the sky and their numerical identifiers. Top panel: region group designations discussed in Section 5.1. Bottom panel: region groups of synchrotron loops discussed in Section 5.2.

optimize the template fitting procedure, we mask regions of the sky that lie along the plane of the Galaxy where components are highly correlated at 1° scales or larger and the $\text{H}\alpha$ template suffers from significant extinction, making the separation of components unreliable. The Galactic plane is masked by first median filtering the C-BASS map on 5° scales, and then masking the brightest 10 per cent of pixels in the filtered map. The Galactic plane mask is shown as the *blue* region in Fig. 1.

Point sources can also be problematic for template fitting as they can dominate over the diffuse background emission, resulting in a highly biased estimate of the amplitudes describing the diffuse components. At lower frequencies, we use the source-subtracted 408 MHz and 4.76-GHz C-BASS maps, thus we only mask the very brightest sources or sources that are found to have large residuals after subtraction. Fig. 1 shows bright sources (>10 Jy at 4.76 GHz; Grmitt et al. 2020) masked by a 2° diameter aperture. There are also some fainter point sources ($S_\nu < 10$ Jy at 4.76 GHz) that leave residuals in the C-BASS map after subtraction; we mask these using a smaller 1° diameter aperture.

At WMAP and *Planck* frequencies, the maps are not confusion-limited since the majority of background radio sources have steep

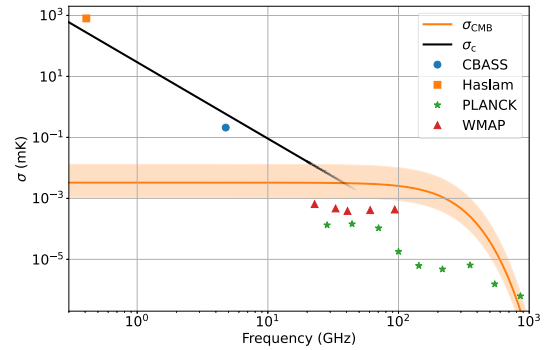


Figure 3. Summary of the mean instrumental pixel noise RMS for each data set (*points*). The *black* line is the confusion noise model given by equation (10), we fade the line at high frequencies as at these frequencies the steep-spectrum background sources are less relevant. The *orange* bounded region shows the range of the residual CMB fluctuations for pixels of approximately 1 deg^2 ($N_{\text{side}} = 64$).

spectra and are generally too faint to detect in the WMAP/*Planck* data. However, there are still a large number of flat-spectrum sources present at high frequencies, and we mask these using the 30-GHz *Planck* catalogue of compact sources (PCCS) (Planck Collaboration XXVI 2016). We mask 893 PCCS sources in the range $50 < S < 1000$ mJy with an aperture of diameter 1.5 , and 628 sources with flux densities $S > 1$ Jy with a 3° wide aperture. Both the PCCS sources and the C-BASS sources described earlier are shown in Fig. 1 as the *orange* regions.

4.4 Regions

For this analysis, we divided the sky into equal-sized regions using the Healpix grid (Górski et al. 2005) on the celestial sphere. We chose to use a region size of $N_{\text{side}} = 4$, which equates to regions with areas of approximately 200 deg^2 . There are a total of 108 regions, which are shown in Fig. 2. The maximum number of $N_{\text{side}} = 64$ pixels within a region is 256, but after masking the number of pixels within each region ranges between 104 and 252 (regions with less than 100 pixels are excluded). The choice of region size is important because regions that are too small have larger spatial correlations between emission types as the template fitting method relies on there being spatial differences between components to work. Whereas larger sized regions become more susceptible to systematics since large scales are generally harder to constrain. Further, larger regions result in less information on the spatial variations across the sky. We found that a region size of $N_{\text{side}} = 4$ was a good balance between these considerations given the resolution of C-BASS data.

4.5 Noise covariances

As described in Section 4.1, we estimate the uncertainties in the fitted coefficients using bootstrapping, and not the intrinsic noise covariances of each map. However, we still need to calculate the noise covariance to correctly weight each pixel. Fig. 3 provides a summary of all the different contributions to the total noise budget at each frequency. We can see from the figure that the instrumental noise is never the dominant source of noise in the maps – except for the 408-MHz data. At higher frequencies, we have neglected contributions to the noise due to confused infrared galaxies. We give a more detailed description of each contribution below.

For this analysis, we assume the covariance matrix N is diagonal and is the sum of contributions from instrumental noise, confused background radio sources, and residual CMB fluctuations. As mentioned in Section 3, the SMICA estimate of the CMB (Planck Collaboration XII 2014) was subtracted from all the maps, therefore we only consider *uncorrelated* CMB residual fluctuations. The noise covariance matrix is therefore constructed as

$$N = N_{\text{noise}} + N_{\delta\text{CMB}} + N_{\text{PS}}, \quad (7)$$

where N_{noise} describes noise contributions from the instruments, $N_{\delta\text{CMB}}$ due to uncorrelated errors in the CMB subtraction, and N_{PS} due to confusion from background radio sources.

Instrument noise covariances are calculated for WMAP using the maps of integration time per pixel (hit maps) and the receiver sensitivities provided in Bennett et al. (2013). For *Planck* and C-BASS, variance maps are calculated during the map-making stage for each pixel and can be used directly. The noise variances for all three surveys are corrected for smoothing of the noise by rescaling the noise by the integral of the Gaussian beam transfer function. For the 408-MHz map, there is no information on the per pixel noise in the map, however, Remazeilles et al. (2015) estimated the noise at $N_{\text{side}} = 512$ (i.e. ≈ 7 arcmin size pixels) to be ≈ 800 mK, which is equivalent to 0.1 mK deg^{-1} .

To estimate the noise due to the randomly (Poisson) distributed background radio sources, we used the compilation of differential source counts for frequencies of 0.1–1000-GHz provided in de Zotti et al. (2010). We calculated the power spectrum of the sources by integrating differential source counts

$$C_\ell = \left(\frac{2k\nu^2}{c^2} \right)^{-2} \int_{S_{\text{min}}}^{S_{\text{max}}} S^2 \left(\frac{dN}{dS} \right) dS, \quad (8)$$

where $\frac{dN}{dS}$ is the model of the differential source counts at a given frequency, k is the Boltzmann constant, c is the speed of light, and ν is the observing frequency. We use an upper limit of $S_{\text{max}} = 1$ Jy to match the flux density at which we mask sources, and a lower limit (S_{min}) that matched each source catalogue’s minimum flux density. To estimate the confusion noise in the map, we then multiply the background source power spectrum from equation (8) by a Gaussian beam transfer function (FWHM = 1°) and integrate over all ℓ as

$$\sigma_c^2 = \frac{\sum_\ell (2\ell + 1) C_\ell B_\ell}{4\pi}, \quad (9)$$

where B_ℓ is the power of the Gaussian beam transfer function. We then fitted a power-law to σ_c^2 measured at each frequency between 1 and 20 GHz to get a model of the confusion noise due to steep-spectrum radio sources

$$\log_{10} \left(\frac{\sigma_c^2}{\text{K}^2} \right) = -5.0 \log_{10} \left(\frac{\nu}{\text{GHz}} \right) - 3.1 + \log_{10} \left(\frac{\theta^2}{\text{deg}^2} \right), \quad (10)$$

where θ is the beam FWHM, and ν is the frequency in GHz. Equation (10) is only an applicable model of confusion up to a few tens of gigahertz, after which the background source population is dominated by flatter-spectrum radio sources (e.g. Healey et al. 2007), and at infrared frequencies the cosmic infrared background becomes the dominant source of confusion (e.g. Guiderdoni et al. 1997). These additional sources of uncertainty are accounted for by the bootstrapping method discussed in Section 4.

In Fig. 3, the contribution of the residual CMB noise exceeds the noise in the data for most of the WMAP and *Planck* frequencies. To calculate the contribution of the residual CMB noise ($N_{\delta\text{CMB}}$), we use the five CMB maps published in Planck Collaboration XII (2014). We calculated each unique difference pair between these maps resulting

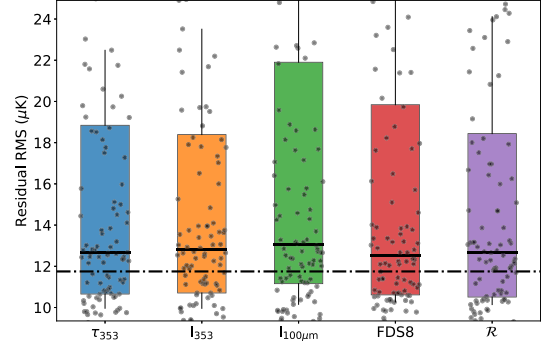


Figure 4. Box-plot of the residual RMS at 22.8 GHz for each region and each dust template. The coloured boxes represent the first and third quartiles of each distribution, and the **bold-black** line is the median of each distribution. The dot-dashed black line indicates the median expected RMS at 22.8 GHz.

in a cube of ten CMB difference maps. We downsampled each difference map from its original resolution ($N_{\text{side}} = 2048$) to the same pixel size as the rest of the data ($N_{\text{side}} = 64$), and stored the variance within each downsampled pixel. We then took the CMB noise contribution to be the mean variance across all of the 108 regions.

5 TEMPLATE FITTING RESULTS

5.1 Dust

Here, we present the template fitting coefficients derived using the dust templates. There are a number of different dust tracers that are available. In this section, we will be comparing five dust tracers (Table 1): The Finkbeiner, Davis & Schlegel (1999) model-8 94 GHz predicted dust brightness map (hereafter FDS8); the IRAS 100 μm map ($I_{100\mu\text{m}}$; Miville-Deschenes & Lagache 2005); the *Planck* integrated dust intensity or dust radiance map (\mathcal{R} ; Planck Collaboration XI 2014); the *Planck* derived thermal dust optical depth at 353 GHz (τ_{353} ; Planck Collaboration XI 2014); and the *Planck* 353-GHz intensity data (I_{353} ; Planck Collaboration I 2020). We use these five dust tracers in this section to see which of them best traces AME, to determine whether AME can be explained by a hard synchrotron component, and to study the distribution of AME emissivity across the sky. Later, in Section 6, we fit spectral models to the dust coefficients presented in this section.

One of the biggest challenges for AME studies has been determining which dust map best traces AME. In order to compare the five different dust tracers, we look at the residual RMS at 22.8 GHz in each region after subtracting our best model for the emission. In the case that the emission is perfectly modelled we expect that the noise in the map will be equivalent to a combination of instrumental, confusion, and residual CMB noise. In Fig. 4, we show the RMS, at 22.8 GHz, of each region after subtracting the best-fitting dust, synchrotron, and free-free templates. We did this for each dust template and find that there is no global preference for any one dust tracer over another on the scales of the region sizes ($\approx 10^\circ$). It is not surprising that we find little difference between the dust tracers since they are all tracing features at high latitudes that are spatially nearby (Green et al. 2019) and tend to share similar environmental conditions (Planck Collaboration XI 2014).

Another long-standing challenge with studies of AME on large scales has been separating it from synchrotron emission (e.g. Gold et al. 2011; Planck Collaboration XXV 2016). AME has a peaked

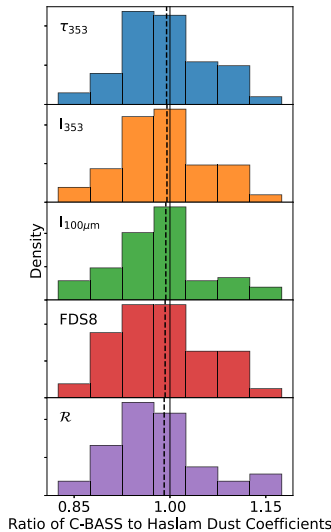


Figure 5. Weighted histograms of the fitted dust coefficients when using the C-BASS 4.76-GHz template over those fitted when using 408-MHz Haslam synchrotron template for each dust tracer at 22.8 GHz. The *dashed* lines indicate the weighted mean for each dust template. The weighted average ratio is consistent with unity for each dust template.

spectrum that can be broadly described by a lognormal distribution centred on 20–30 GHz (e.g. Bonaldi & Ricciardi 2011; Planck Collaboration Int. XII 2013; Stevenson 2014; Cepeda-Arroita et al. 2021). However, at frequencies above the spectral peak, AME can be described reasonably well by just a simple steep-spectrum power law, which can be challenging to separate from the synchrotron spectrum. This has led to the suggestion that Galactic synchrotron emission could be decomposed into two broad synchrotron components. The first being a soft/steep spectrum synchrotron component which is what is observed in the 408-MHz all-sky data, and the second, describing AME, is a dust-correlated hard/flat synchrotron component associated with star formation regions (Bennett et al. 2003; Davies et al. 2006).

If AME is due to a hard/flat spectrum synchrotron component we would expect to find AME in the 4.76-GHz C-BASS data. If this were the case then previous estimates of the dust coefficients that used the 408-MHz synchrotron template to trace synchrotron emission around 20–60 GHz would be significantly different to those reported here due to correlations between the dust and 4.76-GHz synchrotron templates. These differences can be either positive or negative depending on the local relative brightnesses of the synchrotron emission and potential AME at 4.76 GHz. In Fig. 5, we show a weighted histogram of the ratios of the dust coefficients measured using the 4.76-GHz synchrotron template over the 408-MHz template for each dust tracer (excluding a single outlier region – discussed below). We find that the weighted mean ratio is consistent with unity for each template. We find that most individual regions are also consistent, within uncertainties, with no change in the emissivity of AME when changing the synchrotron tracer. We therefore find no evidence that AME is a flat-spectrum synchrotron component.

We find that region 46 (Serpens group – Fig. 2) is the only region to have a significant ($>5\sigma$) change in the ratio of the dust coefficients. Region 46 lies along the northern edge of the North Polar Spur (NPS) and contains both bright diffuse synchrotron and diffuse dust emission. When the synchrotron component is fitted using the 4.76-GHz template the dust coefficient is $(19.5 \pm 1.4) \tau_{353}/\text{K}$, which is more than three times greater than the equivalent when using the

408-MHz template of $(5.9 \pm 1.5) \tau_{353}/\text{K}$. We find that there is a negative correlation between the dust and synchrotron coefficients in this region when using either the 4.76-GHz template ($\rho_{4.76} = -0.58$) or the 408-MHz template ($\rho_{408} = -0.48$), indicating that the pixel brightness distributions in the 408 MHz, 4.76 GHz, and τ_{353} templates are equally correlated. The measured difference in dust emissivity could be due to region selection effects. To test this, we looked at the region again with a larger grid size ($N_{\text{side}} = 2$, or a region of approximately 800 deg^2) and found that the dust emissivity measured using the 408-MHz template of $(17.6 \pm 1.2) \tau_{353}/\text{K}$ is more consistent with the dust emissivity using the 4.76-GHz template of $(19.6 \pm 1.0) \tau_{353}/\text{K}$. The reason for the difference between $N_{\text{side}} = 2$ and $N_{\text{side}} = 4$ when using the 408 MHz template is possibly due to the data processing of the 408-MHz map (Remazeilles et al. 2015) that averages out over a larger region.

In Table 2, we give the measured coefficients for a joint fit to all regions simultaneously (a_{all} – hereafter *all-region fit*). We note that for the I_{353} and FDS8 templates there is no significant difference between the all-region and region average coefficients. However, the all-region τ_{353} estimate is lower by approximately 10 per cent, and the all-sky $I_{100\mu\text{m}}$ and \mathcal{R} fit are systematically higher by almost 50 per cent. The fact that we do not find all dust tracers to be systematically higher or lower than the region averages suggests that this is a real difference between the five dust tracers. This could occur because the all-region fit is sensitive to larger angular scale emission that is effectively filtered out when fitting each region individually.

Comparing the coefficients presented in Table 2 to similar analyses in the literature that used the 408-MHz map to trace Galactic synchrotron emission, we find our results are consistent, again suggesting flat-spectrum synchrotron is not a significant component at frequencies of 5 GHz and higher. For the FDS8 template, previous measurements found the average coefficient at high latitudes to be $(6.6 \pm 0.3) \mu\text{K}/\text{mK}$ at 22.8 GHz (Kp2 mask; Davies et al. 2006). There are also several papers that look at τ_{353} , for which, at high latitudes, Hensley, Draine & Meisner (2016) found the coefficient to be $(7.9 \pm 2.6) \text{K}/\tau_{353}$ at 30 GHz, slightly larger than the average we find here but within the interquartile range of the values. At 22.8 GHz, Planck Collaboration XXV (2016) find τ_{353} to be slightly lower than we find it; $(9.7 \pm 1.0) \text{K}/\tau_{353}$ at high latitudes. Although our results are consistent with most previous measurements we do find that the dust coefficient we measure using \mathcal{R} is 30–40 per cent lower than that in Hensley et al. (2016). We believe this discrepancy is due to the COMMANDER-derived AME map, which is known to be discrepant with other AME measurements at the 30–50 per cent level (Planck Collaboration IV (Planck Collaboration XXV 2016; Planck Collaboration IV 2020; Cepeda-Arroita et al. 2021). Table B1 and Table B2 provide the synchrotron, dust, and free-free coefficients at 22.8 GHz for all regions using the 4.76 GHz, τ_{353} , and $\text{H}\alpha$ ($f_D = 0.33$) templates.

In Fig. 6, we show the AME emissivity defined as the intensity per total hydrogen column density for each region. We can derive the emissivity from the fitted τ_{353} dust parameters by the relation

$$\epsilon_v = 3.1 \left(\frac{a_T}{\text{K}/\tau_{353}} \right) \left(\frac{\sigma_{e,353}}{\tau_{353}/\text{H cm}^{-2}} \right) \left(\frac{\nu}{\text{GHz}} \right)^2 \times 10^4 \text{ Jy sr}^{-1} \text{ cm}^2 \text{ H}^{-1}, \quad (11)$$

where a_T is the fitted dust coefficient, and the average dust opacity at 353 GHz is $\sigma_{e,353} = (7.0 \pm 2.0) \times 10^{-27} \text{ cm}^2 \text{ H}^{-1}$ for $|b| > 15^\circ$ (Planck Collaboration XI 2014). The frequency dependence in equation (11) is due to the conversion from brightness temperature to flux density per steradian. The colours of the markers in Fig. 6

Table 2. Median dust coefficients for the C-BASS 4.76 GHz, WMAP 22.8 GHz and *Planck* 28.4-GHz data for each dust template. The synchrotron component is traced using C-BASS for the WMAP and *Planck* data, and is traced using the 40-MHz map in the C-BASS data. The 25th and 75th percentiles are given as subscripts and superscripts, respectively. The uncertainty given includes both the statistical and calibration uncertainties. For comparison, we include both the weighted average of the regions and the best fit to all regions simultaneously.

	C-BASS 4.76 GHz		WMAP 22.8 GHz		Planck 28.4 GHz		Unit
	$\langle a \rangle$ regions	a_{all}	$\langle a \rangle$ regions	a_{all}	$\langle a \rangle$ regions	a_{all}	
τ_{353}	$3_{-86}^{124} \pm 2$	61 ± 3	$11.5_{10.0}^{15.7} \pm 0.4$	10.0 ± 0.3	$5.8_{5.3}^{8.7} \pm 0.2$	5.3 ± 0.2	K/τ_{353}
I_{353}	$0.2_{-5.0}^{10.1} \pm 0.2$	5.7 ± 0.2	$1.01_{0.87}^{1.29} \pm 0.03$	0.94 ± 0.03	$0.52_{0.43}^{0.69} \pm 0.02$	0.5 ± 0.02	K/K
$I_{100\mu\text{m}}$	$43_{-90}^{320} \pm 7$	178 ± 9	$26.3_{20.6}^{32.7} \pm 0.8$	35.9 ± 1.1	$14.0_{10.7}^{17.7} \pm 0.4$	19.3 ± 0.6	$\mu\text{K}/\text{MJy sr}^{-1}$
FDS8	$1.6_{-41.4}^{80.3} \pm 1.2$	36.5 ± 1.6	$6.9_{5.9}^{8.6} \pm 0.2$	6.4 ± 0.2	$3.5_{2.9}^{4.6} \pm 0.1$	3.4 ± 0.1	K/K
\mathcal{R}	$600_{-2700}^{7000} \pm 130$	3680 ± 160	$600_{480}^{710} \pm 20$	710 ± 20	$310_{260}^{380} \pm 10$	380 ± 12	$\text{K}/(\text{Wm}^{-2} \text{sr}^{-1})$

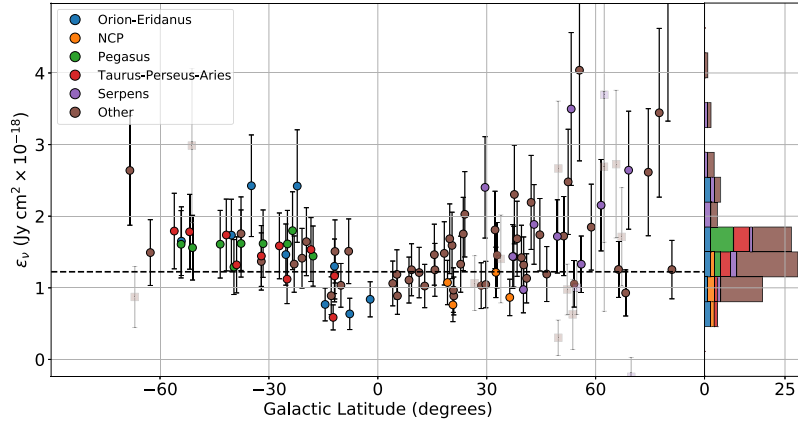


Figure 6. Region-to-region AME emissivity at 22.8 GHz derived using equation (11) and the τ_{353} dust coefficients. Marker colours indicate the regions associated region group as defined in Fig. 2. The weighted mean AME emissivity at 22.8 GHz over all regions is shown with the *dashed* black line. Semi-transparent symbols are for regions that have coefficient SNR < 5. The right-hand panel shows the histogram of the coefficients colour-coded by region group.

indicate which region group each region belongs to, we chose region groups based on known dust features (region group locations are shown in Fig. 2). We found that there is no significant difference in the AME emissivity between these region groups implying that the spinning dust emission origin between region groups is similar.

The mean fitted τ_{353} dust coefficient is $(11.5 \pm 0.4) \text{K}/\tau_{353}$ at 22.8 GHz (Table 2) which gives a mean AME emissivity at high Galactic latitudes of $(1.3 \pm 0.4) \times 10^{-18} \text{Jy sr}^{-1} \text{cm}^2 \text{H}^{-1}$. The weighted mean emissivity across all regions in Fig. 6 at 22.8 GHz is $(1.2 \pm 0.4) \times 10^{-18} \text{Jy sr}^{-1} \text{cm}^2$. We find the emissivity we measure using equation (11) is systematically lower than the theoretical estimates, which at 22.8 GHz can vary between $(3 - 12) \times 10^{-18} \text{Jy sr}^{-1} \text{cm}^2 \text{H}^{-1}$ depending on the environment (e.g. Draine & Lazarian 1998b; Ali-Haïmoud et al. 2009). Although these emissivities are lower than initially expected, they are not beyond the possibility of the spinning dust model given the large number of parameters that can be tuned. Alternatively, the low emissivities could indicate a bias between the AME emissivity and the dust column traced by the τ_{353} map (as well as the other dust tracers). This suggests that the AME emissivity may not be a linear function of the dust column density in high-latitude cirrus regions – we discuss this more in Section 7.1.

We find that the AME emissivity, for most regions, is typically within 1 or 2 σ of the region averaged emissivity. There appears to be a bias where regions with larger uncertainties have larger emissivities (this is apparent in the skewed tail of the distribution shown in Fig. 6).

Most of these regions are associated with latitudes of $b > 50^\circ$, which is perhaps evidence that regions with lower total dust columns have a higher AME emissivity.

Finally, we discuss the measurements of dust-correlated emission measured at 4.76 GHz in the C-BASS map using the τ_{353} dust template. We find that the weighted average of the dust coefficients measured in each region is consistent with zero ($\langle a_{4.76} \rangle_{\text{regions}} = (3 \pm 2) \text{K}/\tau_{353}$). We find some regions around the Galactic North pole do have a significant ($>3\sigma$) detection, but these regions have very little total emission in both the C-BASS and dust maps, and therefore we consider these to be unreliable estimates. When fitting all regions simultaneously we do make a detection of dust-correlated emission in the C-BASS map ($a_{4.76, \text{all}} = (61 \pm 3) \text{K}/\tau_{353}$). When fitting for the dust at 4.76 GHz, we found that the resulting free-free coefficients were 30 per cent lower than when not fitting for the dust emission. There was no significant effect on the synchrotron coefficients. The decrease in the free-free coefficients is likely due to the correlation between dust and the warm ISM at high latitudes (Dobler & Finkbeiner 2008). We therefore attempted fitting for the all-region dust coefficients after first subtracting an estimate of the free-free emission at 4.76 GHz (assuming $T_e = 5000 \text{K}$), we found that this made no significant change to the estimate of the AME emissivity in the C-BASS map. The AME emissivity at 4.76 GHz relative to 22.8 GHz is approximately what would be expected from the AME spectrum, however, there are a large number of potential biases on such large-scales that could account for the detection (e.g.

Table 3. Region averaged and all-region spectral indices between 408 MHz (top panel) and 4.76 GHz (bottom panel) and 22.8-, 28.4-, and 33-GHz data sets. The third and first quartiles of the spectral index distributions are given as superscripts and subscripts, respectively. Uncertainties include both statistical and calibration uncertainties.

	$\langle\beta\rangle$ regions	β_{all}
0.408–4.76 GHz	$-3.04_{-3.16}^{-2.92} \pm 0.02$	-3.02 ± 0.02
0.408–22.8 GHz	$-3.04_{-3.14}^{-2.98} \pm 0.01$	-3.02 ± 0.01
0.408–28.4 GHz	$-3.04_{-3.17}^{-2.98} \pm 0.01$	-3.01 ± 0.01
0.408–33 GHz	$-3.04_{-3.18}^{-2.98} \pm 0.01$	-3.06 ± 0.01
4.76–0.408 GHz	$-2.93_{-3.16}^{-2.90} \pm 0.04$	-3.01 ± 0.04
4.76–22.8 GHz	$-3.10_{-3.32}^{-2.99} \pm 0.02$	-2.92 ± 0.02
4.76–28.4 GHz	$-3.11_{-3.29}^{-3.02} \pm 0.02$	-2.91 ± 0.02
4.76–33 GHz	$-3.09_{-3.29}^{-2.98} \pm 0.02$	-3.01 ± 0.02

residual free–free emission, dust-synchrotron correlation, etc.), so we consider this estimate to be an upper limit.

5.2 Synchrotron

In the frequency range 0.408–22.8 GHz, the spectrum of Galactic synchrotron emission is expected to steepen with frequency due to CRE aging (e.g. Strong et al. 2011), an effect that has been observed in diffuse Galactic synchrotron emission in a number of observations (e.g. Platania et al. 1998; Kogut et al. 2011). In this section, we will assess the curvature of the synchrotron spectrum by modelling the synchrotron spectrum as a simple power-law and looking at the change in the synchrotron spectral index when using either 408 MHz or 4.76 GHz data to trace the Galactic synchrotron emission.

We model the synchrotron spectrum as a power law

$$T(\nu) = A_r \left(\frac{\nu}{\nu_r} \right)^{\beta_s}, \quad (12)$$

where β_s is the spectral index of synchrotron spectrum between a given frequency ν and a reference frequency ν_r , and A_r is the synchrotron amplitude at ν_r . The fitted synchrotron coefficients give a measure of the brightness ratio of the synchrotron emission between the template map (e.g. the 4.76-GHz or 408-MHz maps) and the map to be fitted; the coefficient is therefore defined as

$$a = \frac{T(\nu)}{T(\nu_0)} = \left(\frac{\nu}{\nu_0} \right)^{\beta_s}, \quad (13)$$

where ν_0 is the frequency of the template map. The spectral index can then be found by simply rearranging equation (13):

$$\beta_s = \frac{\log(a)}{\log(\nu/\nu_0)}. \quad (14)$$

There are two systematic biases we have mitigated for when deriving spectral indices using equation (14); details of these biases are given in Section A. Table 3 gives a summary of the spectral indices between the 408-MHz/4.76-GHz synchrotron templates and 22.8, 28.4, and 33 GHz. A full summary of each regions spectral index measured at 22.8 GHz can be found in Table B1.

In Fig. 7, we show the distributions of synchrotron spectral indices derived using equation (14) at 22.8 GHz. The solid regions in the figure are spectral indices for regions where the synchrotron template coefficient derived using the 4.76-GHz template has a signal-to-noise

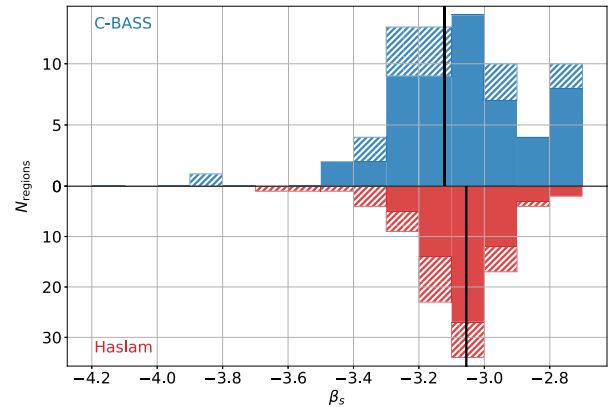


Figure 7. Distributions of spectral indices derived from the 22.8-GHz WMAP *K*-band data with the 4.76-GHz C-BASS and 408-MHz Haslam data sets. The solid lines indicate the spectral index derived from the weighted mean of all the template coefficients. *Hatched* regions indicate spectral indices with signal-to-noise ratios less than 5, and are not used to estimate the mean.

ratio greater than five. The difference in the mean spectral indices (the *solid-black* lines) is $\Delta\beta_{22.8} = -0.06 \pm 0.02$ (Table 3). The steeper spectral indices measured at 4.76 GHz suggest that, on average, Galactic synchrotron emission is steepening at mid-to-high Galactic latitudes with increasing frequency. This supports previous estimates of Galactic synchrotron curvature from historical surveys (Platania et al. 1998), COSMOSOMAS (Fernández-Cerezo et al. 2006), and ARCADE2 (Kogut et al. 2011); there is also some evidence that Galactic synchrotron emission is flattening with increasing frequency in some regions of the Galaxy (Peel et al. 2012). We measure the average synchrotron spectral index between 4.76 and 22.8 GHz to be $\langle\beta_{22.8}\rangle = -3.10 \pm 0.02$, which is more consistent with the spectral index of polarized Galactic synchrotron emission measured between 22.8 and 100 GHz ($\beta_s \approx -3.1$; Dunkley et al. 2009; Fuskeland et al. 2014, 2021) than that measured in intensity using the 408-MHz data ($\beta_s \approx -3.0$; Banday et al. 2003; Davies et al. 2006; Ghosh et al. 2012).

In Fig. 8, we show both the measured absolute spectral index between 4.76 and 22.8 GHz (top panel) and the change in the spectral index at 22.8 GHz when using the 4.76-GHz data instead of the 408-MHz data to trace synchrotron emission (bottom panel). We use colours in the figure to indicate region groups that are associated with known synchrotron loops in the Northern hemisphere using the classification described in Vidal et al. (2015). Fig. 2 shows how these region groups are defined. The *black-dashed* line in the *top* panel of the figure shows the weighted mean over all regions.

In the top panel of Fig. 8, we can see there are several regions with extremely steep spectra – specifically the low latitude Loop I and Loop II regions with spectral indices of $\beta_{\text{Loop I}} = -3.36 \pm 0.05$ (Region-78) and $\beta_{\text{Loop II}} = -3.38 \pm 0.05$ (Region-92), respectively. The steep spectral index at the base of Loop I is especially striking as it implies that either the synchrotron emission within Loop I is flattening at high latitudes with increasing frequency (implying that the CREs at high latitudes are being reaccelerated) or we are measuring the spectral index from a superposition of different components along the line-of-sight at low Galactic latitudes; an argument that has been cited previously as a way of resolving discrepancies in the distance measurements to Loop I (Panopoulou et al. 2021). This is especially interesting since the spectral indices

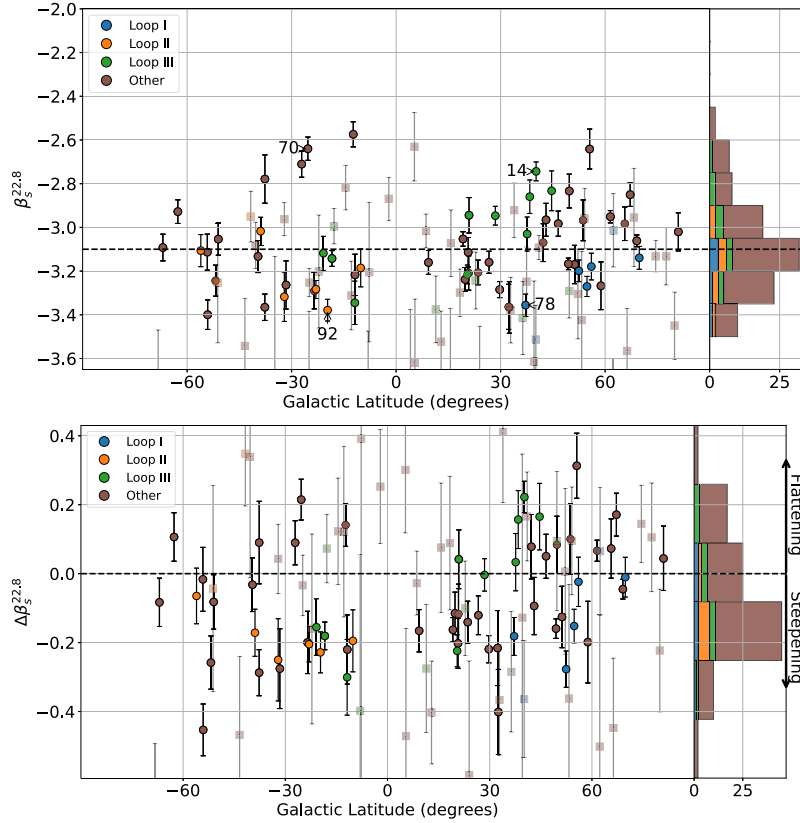


Figure 8. Top panel: The spectral index in each region as measured between 4.76 and 22.8 GHz. Bottom panel: The change in the spectral index at 22.8 GHz when using the 4.76 GHz data instead of the 408-MHz data to trace synchrotron emission, for each region. Colours indicate region groups associated with known Galactic synchrotron loops as defined in Fig. 2. Semi-transparent symbols represent regions that have a spectral index with a signal-to-noise of less than 5 when using either the 408-MHz or 4.76-GHz data. The *black-dashed* line in the top panel gives the weighted mean over all regions. The *black-dashed* line in the bottom panel indicates $\Delta\beta = 0$. Annotations indicate region numbers referenced in the main text.

we measure using the 408-MHz data around Loop I agree with those in the literature (e.g. Davies et al. 2006), implying it is not simply a product of region selection.

Fig. 8 also shows a number of regions where the synchrotron spectrum hardens/flattens at high frequencies. The regions in the southern Galactic hemisphere that show significant flattening ($\sigma > 3$) are associated with bright HII regions such as the Eridanus bubble (Region-70), implying the flattening is due to residual free-free emission in the 4.76-GHz template in these regions. In the northern Galactic hemisphere, Region-14 shows a pronounced flattening of the spectrum, and is associated with synchrotron Loop III. This, like in the case of Loop I, is likely due to a superposition of components along the line of sight in this region, but in this instance it has resulted in a flattening of the synchrotron spectrum.

Several of our regions coincide with the edge of the WMAP haze (Regions: 91, 105, 106), a region of diffuse hard spectrum emission ($\beta \approx -2.5$) in total intensity coincident with the Galactic Centre (Finkbeiner 2004; Dobler & Finkbeiner 2008; Planck Collaboration Int. IX 2013). We find that the average fitted synchrotron spectral index in these regions is consistent with the average for the rest of the sky ($\langle \beta_s \rangle_{\text{Haze}} = -3.11 \pm 0.05$). Likewise, we find that these regions show no significant background residuals (i.e. there is no evidence that the haze component is not being fitted). A full exploration of the haze emission at 4.76 GHz will require the upcoming southern C-BASS survey.

5.3 Free-free

At mid-to-high latitudes, it is challenging to constrain diffuse free-free emission as it is extremely faint except in several nearby star forming regions such as Orion and Eridanus. Free-free emission in the C-BASS map is approximately 25 times brighter than in the WMAP *K*-band map in units of brightness temperature. Even so, for most regions analysed here, we found that the $\text{H}\alpha$ -related coefficients have low S/N due to the free-free emission being a relatively small component relative to synchrotron/AME. The only exceptions were bright ionized regions such as those associated with Orion or the Eridanus loop. Therefore, in order to maximize the signal-to-noise ratio of the free-free emission coefficient at 4.76 GHz, we present just the results for the all-region fit only. We do this for two cases, with and without a correction for dust absorption.

The relationship between the free-free radio brightness and $\text{H}\alpha$ intensity is well defined in regions that have little $\text{H}\alpha$ line-of-sight dust absorption or $\text{H}\alpha$ scattering, and a known electron temperature. The relationship is defined as (Draine 2011)

$$\frac{T_b^{\text{ff}}}{I_{\text{H}\alpha}} = 1512 T_4^{0.517} 10^{0.029/T_4} \nu_{\text{GHz}}^{-2} g_{\text{ff}}, \quad (15)$$

where T_4 is the electron temperature (T_e) in units 10^4 K, and g_{ff} is the Gaunt factor. The Gaunt factor accounts for the quantum mechanical

effects and is approximated by

$$g_{\text{ff}} = \ln \left(\exp \left[5.960 - \frac{\sqrt{3}}{\pi} \ln \left(\nu_{\text{GHz}} T_4^{-3/2} \right) \right] + e \right). \quad (16)$$

Fitting for the free–free emission in the 4.76-GHz map using the 408-MHz map to trace synchrotron emission and the H α map with no correction for dust absorption we find a free–free to H α ratio of $T_{\text{b}}^{\text{ff}}/I_{\text{H}\alpha} = (258 \pm 5) \mu\text{K/R}$,³ which corresponds to an electron temperature of $T_{\text{e}} = (5600 \pm 130) \text{K}$. If we make a correction for dust absorption assuming that the dust and gas are mixed (e.g. $f_{\text{d}} = 0.33$; Dickinson et al. 2003) we find a ratio of $T_{\text{b}}^{\text{ff}}/I_{\text{H}\alpha} = (195 \pm 5) \mu\text{K/R}$ which corresponds to $T_{\text{e}} = (3300 \pm 120) \text{K}$. In both cases, the global average electron temperature is lower than the $6000 < T_{\text{e}} < 8000 \text{K}$ range that is expected from radio-recombination lines (e.g. Alves et al. 2012, 2015) or optical line ratios (e.g. Haffner, Reynolds & Tufté 1999).

Lower than expected estimates of the temperature of the WIM from comparison between radio and H α observations have been measured many times before (Banday et al. 2003; Davies et al. 2006; Dobler & Finkbeiner 2008; Planck Collaboration XXV 2016). There have been several attempts to explain the discrepancy between measured electron temperature of the WIM using continuum free–free emission, and those measured with optical line ratios or RRLs via the physical conditions of the WIM (Dong & Draine 2011; Geyer & Walker 2018), however, the current most favoured explanation is that between 10 to 50 per cent of the observed H α intensity actually comes from secondary scattering from nearby dust clouds (Wood & Reynolds 1999; Witt et al. 2010; Brandt & Draine 2012; Barnes et al. 2015; Planck Collaboration XXV 2016). We estimate the scattering fraction by comparing the mean measured H α coefficients above with the theoretical estimate for H α emission assuming an electron temperature range of $6000 < T_{\text{e}} < 8000 \text{K}$, which corresponds to a range of free–free to H α ratios of $270 < T_{\text{b}}^{\text{ff}}/I_{\text{H}\alpha} < 320 \mu\text{K/R}$ at 4.76 GHz. We can then calculate the fraction of scattered H α light as

$$f_{\text{sc}} = \frac{a_0}{\hat{a}} - 1, \quad (17)$$

where \hat{a} is the measured free–free brightness to H α intensity and a_0 is the theoretical value given by equation (15). We find that if we assume no dust absorption that the fraction of scattered light has a range of $0.04 < f_{\text{sc}} < 0.23$, while after correcting for the dust absorption assuming the dust and gas are mixed we get the range $0.38 < f_{\text{sc}} < 0.64$.

As mentioned before, most individual regions do not have a significant detection of the free–free to H α ratio, except in the Orion–Eridanus regions. If we exclude the Orion–Eridanus regions, the weighted mean of the free–free coefficients for the remaining regions is still less than expected $T_{\text{b}}^{\text{ff}}/I_{\text{H}\alpha} = (266 \pm 6) \mu\text{K/R}$ or a $T_{\text{e}} = (5900 \pm 160) \text{K}$ (assuming no dust absorption). Similarly for just the Orion–Eridanus region, we find the ratio is also low $T_{\text{b}}^{\text{ff}}/I_{\text{H}\alpha} = (243 \pm 9) \mu\text{K/R}$ or $T_{\text{e}} = (5000 \pm 230) \text{K}$. We can therefore see that the underestimate of the free–free to H α ratio seems to affect all of the mid-to-high latitude sky observable by C-BASS. This smaller than expected ratio implies that either the WIM is, in most instances, in front of the dust along most lines of sight and not being absorbed or the fraction of scattered H α light is significantly higher than previously estimated using WMAP/Planck data (Planck Collaboration XXV 2016).

³We also fitted the data using the H α map provided on the NASA LAMBDA website by Finkbeiner (2003) and find a similar ratio of $T_{\text{b}}^{\text{ff}}/I_{\text{H}\alpha} = (241 \pm 9) \mu\text{K/R}$.

6 DUST MODEL FITTING

The fitted dust template coefficients are dependent on the relative brightness of the radio emission relative to the dust template. As such the fitted coefficients are encoded with the relative spectrum of the underlying dust grain population. There are two main components to the spectrum of the fitted dust coefficients: At lower frequencies ($\nu < 100 \text{GHz}$), the dust coefficient spectrum is dominated by contributions from spinning dust emission, while at higher frequencies the spectrum is dominated by contributions from thermal dust emission. With WMAP and Planck data alone it is not possible to constrain the peak frequency of the AME spectrum at high latitudes (e.g. Planck Collaboration X 2016), we therefore use dust template fits to the C-BASS map (fitted using the 408-MHz data to remove the synchrotron component – Section 5.1) to constrain the low frequency turn over in the AME spectrum.

We fit the dust coefficients discussed in Section 5.1 with a two-component model in brightness temperature units defined as

$$a(\nu) = a_{\text{td}}(\nu) + a_{\text{sp}}(\nu), \quad (18)$$

where $a_{\text{td}}(\nu)$ is the contribution to the dust coefficient from thermal dust emission, and $a_{\text{sp}}(\nu)$ is the contribution from spinning dust. We model the thermal dust component as a modified blackbody curve normalized at 353 GHz as

$$a_{\text{td}}(\nu) = A_{\text{td}} \left(\frac{\nu}{\nu_0} \right)^{\beta_{\text{d}}+1} \frac{\exp(\gamma \nu_0) - 1}{\exp(\gamma \nu) - 1}, \quad (19)$$

where A_{td} is the value of the dust coefficient at 353 GHz, $\gamma = h/k_{\text{B}}T_{\text{d}}$ (where T_{d} is the dust temperature) and β_{d} is the thermal dust spectral index. We place Gaussian priors on the thermal dust temperature (T_{d}) and β_{d} parameters of $N(20.3 \pm 5 \text{K})$ and $N(1.59 \pm 0.5)$, respectively, as these parameters have been well constrained by previous analyses (e.g. Planck Collaboration XI 2014; Planck Collaboration X 2016).

We use two models for the AME spectrum. The first jointly fits two spinning dust spectra generated using the SpDust2 model (Ali-Haïmoud et al. 2009; Silsbee, Ali-Haïmoud & Hirata 2011) assuming two different environmental conditions: the cold neutral medium (CNM) and the warm neutral medium (WNM). The typical dust parameters for the CNM and WNM phases were taken from table 1 of Draine & Lazarian (1998b). The approach of combining two SpDust2 spectra to model multiple grain populations along a line of sight has been shown to be effective at modelling the AME spectrum in the past (e.g. Ysard, Miville-Deschênes & Verstraete 2010; Planck Collaboration Int. XV 2014). However, to allow for more flexibility in the model we allow the SpDust2 spectra to be interpolated to different frequency ranges, thus allowing for us to fit for a peak in the spinning dust spectrum. The spinning dust model can be parametrized as

$$a_{\text{sd}}(\nu) = \left(\frac{\nu_0}{\nu} \right)^2 \frac{\sum_i A_i f_i(\nu/\nu_{\text{pi}} \nu_{\text{p0}})}{\sum_i f_i(\nu_0/\nu_{\text{pi}} \nu_{\text{p0}})}, \quad (20)$$

where we are summing over the CNM and WNM models, A_i is the amplitude of each spectrum at the reference frequency of $\nu_0 = 22.8 \text{GHz}$, f_i is the interpolated SpDust2 spectrum functions, and ν_{pi} is the peak frequency of each spectrum. The ν_{p0} parameter is the peak frequency of the input SpDust2 CNM and WNM spectra.

For the SpDust2 model, we must enforce several priors since we still have a limited set of data for constraining the AME spectrum. We follow a similar approach as outlined in Planck Collaboration X (2016), but allow for looser priors due to the additional constraints given by C-BASS at low frequencies. First, we set the condition that the peak frequency of the CNM component is less than the

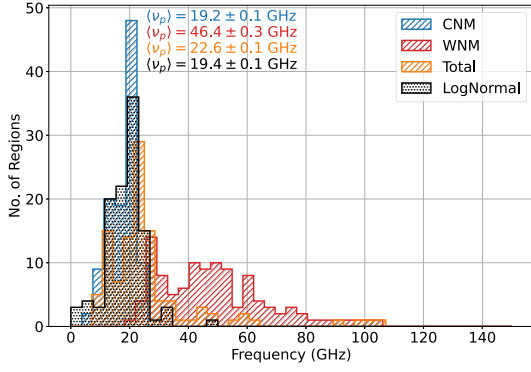


Figure 9. Flux density peak frequencies of the individual CNM and WNM components, and for the combined spinning dust spectra.

Table 4. Best-fitting parameters for the lognormal and two component SpDust2 models. The first uncertainty represents the standard deviation of each distribution shown in Fig. 9 and the second is the uncertainty in the distribution mean.

Parameters	lognormal	Parameters	SpDust2
ν_p [GHz]	$19.4 \pm 6.4 \pm 0.1$	ν_{CNM} (GHz)	$19.2 \pm 4.5 \pm 0.1$
m_{60}	$3.5 \pm 1.7 \pm 0.1$	ν_{WNM} (GHz)	$46.4 \pm 18.5 \pm 0.3$
		ν_p (GHz)	$22.6 \pm 17.7 \pm 0.1$

peak of the WNM component ($\nu_{\text{CNM}} < \nu_{\text{WNM}}$), further we enforce positivity on all components. For the peak frequency of the WNM component, we set a weak Gaussian prior of $N(30 \pm 15\text{GHz})$ to ensure that the WNM component is not biased to fit the thermal dust emission. For the peak frequency of the CNM, we enforce no prior, allowing for the data to drive the determination of the peak frequency.⁴

For the second model, we use a two-parameter lognormal distribution, which has been shown to well characterize the AME spectrum (Bonaldi et al. 2007; Stevenson 2014; Cepeda-Arroita et al. 2021). Here, we use the model first introduced by Bonaldi et al. (2007) of

$$\log(a_{\text{sd}}) = - \left(\frac{m_{60} \log(\nu_p)}{\log(\nu_p/60 \text{ GHz})} \right) \log \left(\frac{\nu}{23 \text{ GHz}} \right) + \frac{m_{60}}{2 \log(\nu_p/60 \text{ GHz})} [\log(\nu/1 \text{ GHz})^2 - \log(23/\text{GHz})^2] + 2 \log(\nu/23 \text{ GHz}) + \log(A), \quad (21)$$

where ν_p is the peak frequency of the spectrum, A is the amplitude at 23 GHz and m_{60} is the spectral index at 60 GHz. As with the SpDust2 model, we enforce positivity for all parameters, we also must enforce that the peak frequency is less than 60 GHz since equation (21) is not defined at 60 GHz. We use no Gaussian priors on the parameters.

In Fig. 9, we show the best-fitting peak frequencies for both the SpDust2 and lognormal models in flux density units.⁵ For the SpDust2 model, we also show the fitted CNM and WNM components peak frequencies. We find that the median peak frequency of the AME flux density spectrum for the SpDust2 and lognormal models agree on average at (19.4 ± 0.1) GHz and (22.6 ± 0.1) GHz, respectively (see Table 4). Similar peak frequencies for high latitudes regions

⁴Fits are performed using the Affine Invariant Markov chain Monte Carlo Ensemble sampler EMCEE (Foreman-Mackey et al. 2013).

⁵The spinning dust spectrum is not peaked in brightness temperature units.

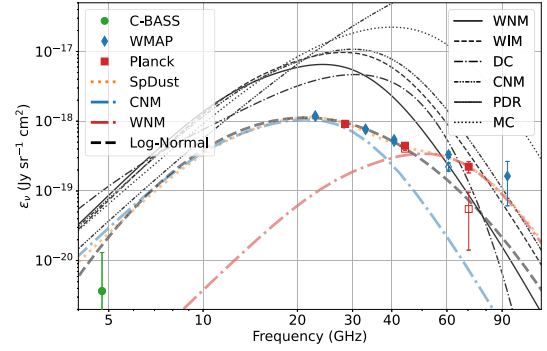


Figure 10. AME emissivity spectrum showing the best-fitting SpDust2 and lognormal models to the weighted average dust coefficients over all regions. The 4.76-GHz C-BASS data are represented by the green circles, the blue diamonds are WMAP, and the red squares are Planck. Solid markers are associated with SpDust2 model fit, and hollow markers with the lognormal fit. Six SpDust2 spinning dust spectra are shown for generic environments: WNM, WIM, dark clouds (DC), CNM, photodissociation regions (PDR), and molecular clouds (MC).

($|b| > 10^\circ$) were found by the Planck Commander analysis (Planck Collaboration XXV 2016), but the Gould belt region was found to have a higher mean peak frequency of (25.5 ± 1.5) GHz (Planck Collaboration Int. XII 2013). Comparing the reduced chi-squared (χ_r^2) of each model shows no strong preference for the more complex three-parameter SpDust2 model ($\chi_r^2 = 2.4$) over the two-parameter lognormal model ($\chi_r^2 = 2.9$).

In Fig. 10, we show the best-fitting SpDust2 and lognormal models fitted to the weighted average dust coefficients in units of emissivity (i.e. brightness per unit column density – see equation 11) with the estimate of the thermal dust contribution subtracted. The 4.76-GHz C-BASS data are critical for constraining the AME spectrum in these plots as they constrain the low frequency turnover. Without C-BASS, there is effectively no constraint on the AME peak frequency at high latitudes without using strong priors (Planck Collaboration XXV 2016). These constraints could be further improved by including data from the QUIJOTE 10–20-GHz northern sky survey (e.g. Génova-Santos et al. 2015).

Fig. 10 shows our estimates of the AME emissivity using the τ_{353} template alongside SpDust2 spinning dust spectra for six generic environments based on the parameters in Draine & Lazarian (table 3, 1998b). We find that the measured emissivities are approximately an order-of-magnitude lower than the predictions from the SpDust2 models. However, this discrepancy can be explained by a number of factors mostly related to the calculation of the dust column density required to estimate the AME emissivity. Taking into account all factors, the differences between the AME emissivity, we measure and the predictions from the generic models can be explained. We will discuss this in more detail in Section 7.1.

7 DISCUSSION

We have shown how using the C-BASS 4.76-GHz data in place of the 408-MHz data to trace synchrotron emission in the WMAP and Planck maps results in very little change in the dust emissivity measured around 30 GHz. We have also shown how C-BASS data suggests that on average the synchrotron spectrum is steepening at high frequencies. In this section, we will discuss these findings in the wider context of findings given in the literature.

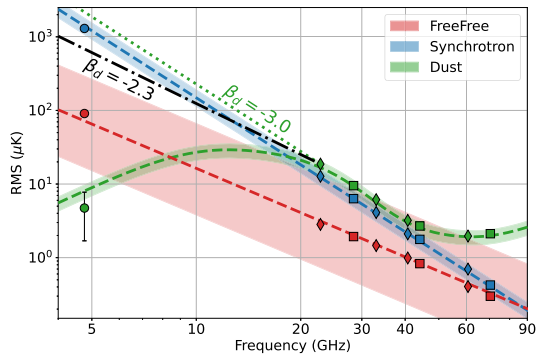


Figure 11. RMS fluctuations spectrum in Rayleigh–Jeans units for all foreground components at 1° resolution. The symbols are the product of the weighted average coefficients and the template RMS with synchrotron as blue, AME and thermal dust as green, and free–free as red. The green dashed curve is the best-fitting spDust2 plus thermal dust model, the blue dashed curve is a power law with spectral index $\beta_s = -3.0$ (from Table 3, and the red dashed curve is the best-fitting power-law free–free model. The shaded regions represent the region-to-region variations by scaling the models to the upper and lower percentiles of the region values at 22.8 GHz for dust and synchrotron, and 4.76 GHz for free–free. We also included the green dashed line indicating the dust spectral index between 22.8 and 40 GHz, and the black dash–dotted line to represent a flat synchrotron spectrum. Diamonds are WMAP, squares are Planck, and circles are C-BASS.

7.1 High latitude AME

One of the earliest detections of AME was at high Galactic latitudes (Kogut et al. 1996) yet confirming the nature and origin of AME at high latitudes has proven to be more challenging than for individual compact objects due to the lack of all-sky surveys between 2 GHz and WMAP/Planck frequencies. As such, it is somewhat more difficult to rule out alternative AME hypotheses such as a dust-correlated hard/flat spectrum synchrotron component that is associated with Galactic star formation (Bennett et al. 2003). A clear test to verify whether there is a flat spectrum synchrotron component that correlates with dust would be to observe such a feature in a higher frequency tracer of synchrotron. Peel et al. (2012) looked for evidence of a hard synchrotron component using 2.3-GHz data but they found no significant evidence for its presence. We find a similar result using C-BASS (as discussed in Section 5.1). Although there is a tentative detection of AME when fitting all regions simultaneously, it is found to have a rising spectrum between 4.76 and 22.8 GHz which is inconsistent with flat-spectrum synchrotron.

In Fig. 11, we show the spectrum of the region averaged coefficients for synchrotron, dust, and free–free emission scaled by the RMS of the associated templates in each region. In the figure, we are using the τ_{353} template for the dust, and the 4.76-GHz template for the synchrotron emission. By doing this, we are able to directly compare the relative brightnesses of each emission component. The spectral index of the dust emission between 22.8 and 40 GHz is $\beta \approx -3$ (shown in the figure as the green dashed line) shows that if the dust emission can be modelled by a power law it would overestimate the limits placed on the AME spectrum by more than two orders of magnitude. We also extrapolate the amplitude of the dust spectrum at 22.8 GHz using a power-law spectrum with $\beta = -2.3$ (black dot–dashed line) indicative of flat-spectrum synchrotron, but still find that this greatly exceeds the limits set by C-BASS. Given these results, high latitude AME cannot be explained by a flat-spectrum synchrotron component, and strongly favours the spinning dust hypothesis of AME.

Next, in Section 5.1, we found that the spinning dust component is traced equally well by all of the dust tracers that we used. This is somewhat of a contradiction to the findings of Hensley et al. (2016) where they find that spinning dust emission most strongly correlates with the Planck derived radiance map. However, there are several differences between the two analyses; Hensley et al. (2016) compared the 30-GHz spinning dust map derived from the Commander analysis (Planck Collaboration XXV 2016) to the radiance map across all pixels simultaneously, while we are using the original WMAP and Planck data in approximately 100 deg^2 patches of the sky. Also interesting to note is that our τ_{353} coefficient is smaller than they report, while our radiance coefficient is larger. These discrepancies are hard to reconcile; however, at high latitudes the Commander spinning dust map is known to be limited due to difficulties in separating the spinning dust from diffuse free–free and synchrotron components, sometimes overestimating and sometimes underestimating the AME by approximately 30–40 per cent (Planck Collaboration XXV 2016; Cepeda-Arroita et al. 2021), which is of order the differences we see between our coefficients and those given in Hensley et al. (2016).

The environmental conditions of the high latitude regions, we are looking at are known to be similar (Planck Collaboration XI 2014), possibly owing to the dust in all of these regions being located relatively nearby (within approximately 0.5 kpc, Green et al. 2019). The spinning dust spectrum is not expected to be very sensitive to the interstellar radiation field (Ali-Haïmoud et al. 2009; Ysard et al. 2010), however, in some AME sources the ISRF intensity has been found to correlate well with AME intensity (Tibbs et al. 2011; Tibbs, Paladini & Dickinson 2012). Planck Collaboration Int. XV (2014) found that there is a limited correlation between AME emissivity, and AME peak frequency with the ISRF, which may be due to the emission from very small grains (VSGs) and PAHs being proportional to the ISRF strength (Sellgren et al. 1985). The relative strength of the ISRF can be parametrized by $G_0 = (T_D/17.5 \text{ K})^{4+\beta_D}$ (Mathis, Mezger & Panagia 1983), the average value of G_0 for Galactic latitudes of $|b| > 15^\circ$ is $G_0 = 2.3$ (Table 3; Planck Collaboration XI 2014), which is higher than the typical G_0 found in denser, discrete sources nearer the Galactic plane (Planck Collaboration Int. XV 2014). This implies that the high latitude dust clouds, though they may share a common environment with each other, is atypical of the environments associated with other sources of AME. One particularly interesting exception is the ρ Ophiuchi molecular cloud that has a similar ISRF to high latitude clouds (Planck Collaboration Int. XV 2014), and has a broad AME spectrum similar to Fig. 10 (e.g. Planck Collaboration XX 2011). The AME in ρ Ophiuchi has been found to be associated with the PDR along the western edge of the cloud (Casassus et al. 2008, 2021), which may indicate that the AME in high latitude dust clouds originates from similar PDR-like environments.

The measured AME emissivities shown in Fig. 10 were found to be an order-of-magnitude lower than the generic environment spinning dust models (the black lines in the figure). On the other hand, earlier analyses found a much better agreement with the models to within a factor of a few (e.g. Draine & Lazarian 1998a; Finkbeiner 2004), which can be easily accounted for by adjusting the environmental parameters. Nevertheless, much of the difference in emissivities with previous analyses can be accounted for by our use of τ_{353} as a dust tracer. Most earlier analyses used the 100- μm IRAS map as a tracer and a column density calibration of $0.85 \times 10^{-20} \text{ MJy sr}^{-1} \text{ cm}^2$ (Boulanger & Perault 1988), which we find results in differences in the column density with τ_{353} (Planck Collaboration XI 2014) by a factor of ≈ 2 . Additionally, early analyses typically fitted for the

full sky as opposed to smaller regions, and indeed we find that our all-region fit for $I_{100\mu\text{m}}$ is higher than the region average by approximately 50 per cent. Together these effects bring our results into approximate agreement with previous results.

Nevertheless, our AME emissivities are still lower than the predictions of the spinning dust model. We first note that the spinning dust models are for generic interstellar environments using the parameters suggested in Draine & Lazarian (1998b), which need to be tuned to fit the observations. An order-of-magnitude can easily be achieved as demonstrated by Vidal et al. (2020). Another important consideration is the averaging of the dust column (and also other quantities) over the regions, which may not be easily characterized by a single SpDust2 model parametrization. For example, if most of the AME originates on small scales, but on large scales there is none, then we would be underestimating the emitting dust column. To quantify this effect will require a multiscale analysis of a known AME emitting region, which we will investigate in a future work.

7.2 Synchrotron curvature

It has been known for some time that synchrotron spectra exhibit some degree of curvature. At frequencies between 100 MHz and 1 GHz the typical spectral index of synchrotron emission is $\beta_s = -2.7$ (Lawson et al. 1987; Platania et al. 1998, 2003), while at frequencies between 408 MHz and 23 GHz the spectral index is $-3.2 < \beta_s < -2.9$ (Banday et al. 2003; Davies et al. 2006; Gold et al. 2011; Ghosh et al. 2012). Previous attempts to measure the spectral index between microwave frequencies and 1–2-GHz surveys have not found strong evidence for an increase in the curvature of the synchrotron spectrum (Peel et al. 2012).

The Galactic synchrotron spectrum tends to flatten at frequencies below <10 GHz (Lawson et al. 1987; Platania et al. 1998; Rogers & Bowman 2008) in line with the expectations of CRE propagation models with a general steepening of the spectrum with increasing Galactic latitude indicative of CRE aging (Orlando & Strong 2013). In Section 5.2, we find that the synchrotron spectrum between 4.76 and 22.8 GHz is steeper than the spectrum between 0.408 and 22.8 GHz by $\Delta\beta_s = -0.06 \pm 0.02$ when averaged across all regions. For the all-region fits, we generally find flatter spectral indices; we tested to see if this could be driven by the flatter spectral indices of the North Polar Spur by repeating the analysis with this region masked but found the spectral index with and without the North Polar Spur to be consistent. This difference is possibly due to systematic errors on large scales or even real Galactic emission – we intend to investigate this further in the future.

8 CONCLUSION

In this study of Galactic AME, synchrotron, and free–free emission using the C-BASS North data we have divided the sky into a HEALPIX grid of $N_{\text{side}} = 4$ or regions of order 200 deg^2 and applied the template fitting technique.

The major result from this study is that we find the fitted dust coefficients around ≈ 30 GHz that trace AME do not significantly change (<1 per cent on average) when using the C-BASS 4.76-GHz map to trace the underlying synchrotron emission instead of the 408-MHz synchrotron template. Further, we find that there is very little evidence for AME at 4.76 GHz and place an upper limit on the emissivity of $\epsilon_{4.76\text{GHz}} < (2.9 \pm 0.2) \times 10^{-19} \text{ Jy sr}^{-1} \text{ cm}^2 \text{ H}^{-1}$ from an all-region fit. Together these two conclusions strongly disfavour AME at high Galactic latitudes being generated by a hard/flattened synchrotron component, and prefer instead that spinning dust is

the origin of AME. We find that the fitted AME spectrum is well described by peaked spectrum models with a median peak frequency of (22.6 ± 0.1) GHz (in flux density units) when fitted using a two component SpDust2 model and (19.4 ± 0.1) GHz when fitted using a lognormal model, implying that the environment of high latitude cirrus clouds is different to those found in other sources of AME, which tend to peak around ~ 30 GHz.

We have found that when using the C-BASS 4.76-GHz data to trace synchrotron on scales of ≈ 10 the synchrotron spectrum steepens at high frequencies by $\Delta\beta_s = -0.06 \pm 0.02$ when the reference frequency is changed from 4.76 GHz to 408 MHz. We also found that some regions such as Loop I exhibit substantial steepening at high frequencies, with the base of Loop I having an extreme spectral index of $\beta_s = -3.36 \pm 0.05$. However, in general, the typical differences between the spectral indices at 22.8 GHz derived using the 408-MHz ($<\beta_s >_{408} = 3.04 \pm 0.01$) or 4.76-GHz C-BASS ($<\beta_s >_{4.76} = -3.1 \pm 0.02$) data are small, and we find no evidence for a hard spectrum synchrotron component (that would result in a flattening of the spectrum at high frequencies). Therefore, extrapolation of the Galactic synchrotron to high frequencies remains a reasonable model, which is important for CMB foreground removal.

For free–free emission, we put new constraints on the free–free brightness to $\text{H}\alpha$ intensity using the 4.76-GHz C-BASS data. Due to the faintness of the free–free emission at intermediate and high Galactic latitudes, we were only able to get a significant detection on the free–free/ $\text{H}\alpha$ ratio when performing a fit across all region simultaneously, or by selecting bright HII structures within the Orion–Eridanus regions. We tested fitting for the free–free emission using $\text{H}\alpha$ templates with either no dust absorption correction and a dust absorption correction assuming a dust mixing fraction of $f_D = 0.33$ and find electron temperatures of $T_e = (5600 \pm 130)$ K and $T_e = (3300 \pm 120)$ K, respectively. The measured electron temperatures are found to be systematically low when compared to estimates from radio recombination lines (Paladini, Davies & De Zotti 2004; Alves et al. 2012, 2015) and optical line ratios (e.g. Haffner et al. 1999). Assuming that the true electron temperature of the warm ISM is within the range $6000 < T_e < 8000$ K, we estimate that the degree of $\text{H}\alpha$ scattered light (Wood & Reynolds 1999; Witt et al. 2010) within the $\text{H}\alpha$ template is either $0.04 < f_{\text{sc}} < 0.23$ (no dust absorption) or $0.38 < f_{\text{sc}} < 0.64$ ($f_D = 0.33$).

Finally, we have demonstrated that the C-BASS data are an invaluable tool for studying large-scale structures in the ISM. In the future, we intend to extend this analysis by looking in more detail at the diffuse ionized gas component of the ISM and placing more rigorous constraints on $\text{H}\alpha$ scattering and HII electron temperatures within the ISM. Further, we wish to extend the technique to include polarization templates of Galactic emission, with the intention of testing magnetic dust emission models of AME and placing more stringent limits on the polarization fraction of AME.

ACKNOWLEDGEMENTS

We thank the referee, Unni Fuskeland, for their useful comments and suggestions that have helped to greatly improve the quality of this paper. The C-BASS project (<http://cbass.web.ox.ac.uk>) is a collaboration between Oxford and Manchester Universities in the UK, the California Institute of Technology in the USA, Rhodes University, UKZN and the South African Radio Observatory in South Africa, and the King Abdulaziz City for Science and Technology (KACST) in Saudi Arabia. It has been supported by the NSF awards AST-0607857, AST-1010024, AST-1212217, and AST-1616227, and NASA award NNX15AF06G, the University of Oxford, the

Royal Society, STFC, and the other participating institutions. This research was also supported by the South African Radio Astronomy Observatory, which is a facility of the National Research Foundation, an agency of the Department of Science and Technology. We would like to thank Russ Keeney for technical help at OVRO. SEH, CD, and JPL acknowledge support from the STFC Consolidated Grant (ST/P000649/1). CD thanks the California Institute of Technology for their hospitality and hosting during several extended visits. We make use of the HEALPix package (Górski et al. 2005), IDL astronomy library (Landsman 1993) and Python astropy (Astropy Collaboration et al. 2013, 2018), MATPLOTLIB (Hunter 2007), NUMPY (Harris et al. 2020), HEALPY (Górski et al. 2005; Zonca et al. 2019), EMCEE (Foreman-Mackey et al. 2013), and SCIPY (Virtanen et al. 2020) packages. This research has made use of the NASA/IPAC Extragalactic Database (NED) which is operated by the Jet Propulsion Laboratory, California Institute of Technology, under contract with the National Aeronautics and Space Administration.

DATA AVAILABILITY

The northern C-BASS intensity and polarization data are not currently available, but will be released following the publication of the upcoming survey paper (Taylor et al., in preparation). Full tables of template fitting coefficients will be made available online upon request.

REFERENCES

- Ali-Haïmoud Y., Hirata C. M., Dickinson C., 2009, *MNRAS*, 395, 1055
- Alves M. I. R., Davies R. D., Dickinson C., Calabretta M., Davis R., Staveley-Smith L., 2012, *MNRAS*, 422, 2429
- Alves M. I. R., Calabretta M., Davies R. D., Dickinson C., Staveley-Smith L., Davis R. J., Chen T., Barr A., 2015, *MNRAS*, 450, 2025
- Astropy Collaboration, 2013, *A&A*, 558, A33
- Astropy Collaboration, 2018, *AJ*, 156, 123
- Banday A. J., Dickinson C., Davies R. D., Davis R. J., Górski K. M., 2003, *MNRAS*, 345, 897
- Barnes J. E., Wood K., Hill A. S., Haffner L. M., 2015, *MNRAS*, 447, 559
- Bennett C. L. et al., 2003, *ApJS*, 148, 97
- Bennett C. L. et al., 2013, *ApJS*, 208, 20
- Berkhuijsen E. M., 1972, *A&AS*, 5, 263
- Bonaldi A., Ricciardi S., 2011, *MNRAS*, 414, 615
- Bonaldi A., Ricciardi S., Leach S., Stivoli F., Baccigalupi C., de Zotti G., 2007, *MNRAS*, 382, 1791
- Boulanger F., Perault M., 1988, *ApJ*, 330, 964
- Brandt T. D., Draine B. T., 2012, *ApJ*, 744, 129
- Calabretta M. R., Staveley-Smith L., Barnes D. G., 2014, *PASA*, 31, e007
- Carretti E. et al., 2019, *MNRAS*, 489, 2330
- Casassus S. et al., 2008, *MNRAS*, 391, 1075
- Casassus S., Vidal M., Arce-Tord C., Dickinson C., White G. J., Burton M., Indermuehle B., Hensley B., 2021, *MNRAS*, 502, 589
- Cepeda-Arroita R. et al., 2021, *MNRAS*, 503, 2927
- Davies R. D., Dickinson C., Banday A. J., Jaffe T. R., Górski K. M., Davis R. J., 2006, *MNRAS*, 370, 1125
- de Oliveira-Costa A., Kogut A., Devlin M. J., Netterfield C. B., Page L. A., Wollack E. J., 1997, *ApJ*, 482, L17
- de Oliveira-Costa A., Tegmark M., Gaensler B. M., Jonas J., Landecker T. L., Reich P., 2008, *MNRAS*, 388, 247
- de Zotti G., Massardi M., Negrello M., Wall J., 2010, *A&A Rev.*, 18, 1
- Dickinson C., Davies R. D., Davis R. J., 2003, *MNRAS*, 341, 369
- Dickinson C. et al., 2018, *New Astron. Rev.*, 80, 1
- Dickinson C. et al., 2019, *MNRAS*, 485, 2844
- Dobler G., Finkbeiner D. P., 2008, *ApJ*, 680, 1235
- Dong R., Draine B. T., 2011, *ApJ*, 727, 35
- Draine B. T., 2011, *Physics of the Interstellar and Intergalactic Medium*. Princeton Univ. Press, Princeton
- Draine B. T., Lazarian A., 1998a, *ApJ*, 494, L19
- Draine B. T., Lazarian A., 1998b, *ApJ*, 508, 157
- Dunkley J. et al., 2009, *ApJS*, 180, 306
- Efron B., 1979, *Acoustical Soc. America J.*, 7, 1
- Efron B., Tibshirani R., 1986, *Statistical Sci.*, 1, 54
- Eriksen H. K., Jewell J. B., Dickinson C., Banday A. J., Górski K. M., Lawrence C. R., 2008, *ApJ*, 676, 10
- Fernández-Cerezo S. et al., 2006, *MNRAS*, 370, 15
- Finkbeiner D. P., 2003, *ApJS*, 146, 407
- Finkbeiner D. P., 2004, *ApJ*, 614, 186
- Finkbeiner D. P., Davis M., Schlegel D. J., 1999, *ApJ*, 524, 867
- Foreman-Mackey D., Hogg D. W., Lang D., Goodman J., 2013, *PASP*, 125, 306
- Fuskeland U., Wehus I. K., Eriksen H. K., Naess S. K., 2014, *ApJ*, 790, 104
- Fuskeland U. et al., 2021, *A&A*, 646, A69
- Génova-Santos R. et al., 2015, *MNRAS*, 452, 4169
- Geyer M., Walker M. A., 2018, *MNRAS*, 481, 1609
- Ghosh T., Banday A. J., Jaffe T., Dickinson C., Davies R., Davis R., Gorski K., 2012, *MNRAS*, 422, 3617
- Gold B. et al., 2011, *ApJS*, 192, 15
- Górski K. M., Hivon E., Banday A. J., Wandelt B. D., Hansen F. K., Reinecke M., Bartelmann M., 2005, *ApJ*, 622, 759
- Green G. M., Schlafly E., Zucker C., Speagle J. S., Finkbeiner D., 2019, *ApJ*, 887, 93
- Gregory P. C., Scott W. K., Douglas K., Condon J. J., 1996, *ApJS*, 103, 427
- Gruitt R. D. P. et al., 2020, *MNRAS*, 496, 1941
- Guiderdoni B., Bouchet F. R., Puget J.-L., Lagache G., Hivon E., 1997, *Nature*, 390, 257
- Guidi F., Quijote Collaboration, 2020, in *Contributions to the XIV.0 Scientific Meeting (virtual) of the Spanish Astronomical Society*. Sociedad Espanola de Astronomia, Univ. Barcelona, Barcelona, p. 45
- Haffner L. M., Reynolds R. J., Tuftes S. L., 1999, *ApJ*, 523, 223
- Harris C. R. et al., 2020, *Nature*, 585, 357
- Haslam C. G. T., Salter C. J., Stoffel H., Wilson W. E., 1982, *A&AS*, 47, 1
- Healey S. E., Romani R. W., Taylor G. B., Sadler E. M., Ricci R., Murphy T., Ulvestad J. S., Winn J. N., 2007, *ApJS*, 171, 61
- Hensley B. S., Draine B. T., Meisner A. M., 2016, *ApJ*, 827, 45
- Holler C. M. et al., 2013, *IEEE Trans. Antennas Propag.*, 61, 117
- Hunter J. D., 2007, *Comput. Sci. Eng.*, 9, 90
- Irfan M. O. et al., 2015, *MNRAS*, 448, 3572
- Jonas J. L., Baart E. E., Nicolson G. D., 1998, *MNRAS*, 297, 977
- Jones M. E. et al., 2018, *MNRAS*, 480, 3224
- King O. G. et al., 2014, *MNRAS*, 438, 2426
- Kogut A., Banday A. J., Bennett C. L., Gorski K. M., Hinshaw G., Smoot G. F., Wright E. I., 1996, *ApJ*, 464, L5
- Kogut A. et al., 2011, *ApJ*, 734, 4
- Landsman W. B., 1993, in *Hanisch R. J., Brissenden R. J. V., Barnes J., eds, ASP Conf. Ser., Vol. 52, Astronomical Data Analysis Software and Systems II*. Astron. Soc. Pac., San Francisco, p. 246
- Lawson K. D., Mayer C. J., Osborne J. L., Parkinson M. L., 1987, *MNRAS*, 225, 307
- Leitch E. M., Readhead A. C. S., Pearson T. J., Myers S. T., 1997, *ApJ*, 486, L23
- Mathis J. S., Mezger P. G., Panagia N., 1983, *A&A*, 500, 259
- Mingaliev M. G., Sotnikova Y. V., Bursov N. N., Kardashev N. S., Larionov M. G., 2007, *Astron. Rep.*, 51, 343
- Miville-Deschenes M.-A., Lagache G., 2005, *ApJS*, 157, 302
- Orlando E., Strong A., 2013, *MNRAS*, 436, 2127
- Paladini R., Davies R. D., De Zotti G., 2004, *MNRAS*, 347, 237
- Panopoulou G. V., Dickinson C., Readhead A. C. S., Pearson T. J., Peel M. W., 2021, *ApJ*, 922, 210
- Pauliny-Toth I. K., Shakeshaft J. R., 1962, *MNRAS*, 124, 61
- Peel M. W., Dickinson C., Davies R. D., Banday A. J., Jaffe T. R., Jonas J. L., 2012, *MNRAS*, 424, 2676
- Planck Collaboration XX, 2011, *A&A*, 536, A20
- Planck Collaboration XXI, 2011, *A&A*, 536, A21

- Planck Collaboration XI, 2014, *A&A*, 571, A11
 Planck Collaboration Int. XII, 2013, *A&A*, 557, A33
 Planck Collaboration X, 2016, *A&A*, 594, A10
 Planck Collaboration XXV, 2016, *A&A*, 594, A25
 Planck Collaboration XXVI, 2016, *A&A*, 594, A26
 Planck Collaboration I, 2020, *A&A*, 641, A1
 Planck Collaboration IV, 2020, *A&A*, 641, A4
 Planck Collaboration Int. IX, 2013, *A&A*, 554, A139
 Planck Collaboration XII, 2014, *A&A*, 571, A12
 Planck Collaboration Int. XV, 2014, *A&A*, 565, A103
 Planck Collaboration Int. XXII, 2015, *A&A*, 576, A107
 Platania P., Bensadoun M., Bersanelli M., De Amici G., Kogut A., Levin S., Maino D., Smoot G. F., 1998, *ApJ*, 505, 473
 Platania P., Burigana C., Maino D., Caserini E., Bersanelli M., Cappellini B., Mennella A., 2003, *A&A*, 410, 847
 Reich P., Testori J. C., Reich W., 2001, *A&A*, 376, 861
 Reif K., Reich W., Steffen P., Müller P., Weiland H., 1987, *Mitt. Astron. Ges.*, 70, 419
 Remazeilles M., Dickinson C., Banday A. J., Bigot-Sazy M.-A., Ghosh T., 2015, *MNRAS*, 451, 4311
 Remazeilles M., Dickinson C., Eriksen H. K. K., Wehus I. K., 2016, *MNRAS*, 458, 2032
 Rogers A. E. E., Bowman J. D., 2008, *AJ*, 136, 641
 Schlegel D. J., Finkbeiner D. P., Davis M., 1998, *ApJ*, 500, 525
 Sellgren K., Allamandola L. J., Bregman J. D., Werner M. W., Wooden D. H., 1985, *ApJ*, 299, 416
 Silsbee K., Ali-Haïmoud Y., Hirata C. M., 2011, *MNRAS*, 411, 2750
 Stevenson M. A., 2014, *ApJ*, 781, 113
 Strong A. W., Orlando E., Jaffe T. R., 2011, *A&A*, 534, A54
 Sutton D. et al., 2010, *MNRAS*, 407, 1387
 Tibbs C. T. et al., 2011, *MNRAS*, 418, 1889
 Tibbs C. T., Paladini R., Dickinson C., 2012, *Adv. Astron.*, 2012, 124931
 Tibbs C. T., Scaife A. M. M., Dickinson C., Paladini R., Davies R. D., Davis R. J., Grainge K. J. B., Watson R. A., 2013, *ApJ*, 768, 98
 Vidal M., Dickinson C., Davies R. D., Leahy J. P., 2015, *MNRAS*, 452, 656
 Vidal M., Dickinson C., Harper S. E., Casassus S., Witt A. N., 2020, *MNRAS*, 495, 1122
 Virtanen P. et al., 2020, *Nat. Meth.*, 17, 261
 Weiland J. L. et al., 2011, *ApJS*, 192, 19
 Witt A. N., Gold B., Barnes F. S., III, DeRoo C. T., Vijn U. P., Madsen G. J., 2010, *ApJ*, 724, 1551
 Wood K., Reynolds R. J., 1999, *ApJ*, 525, 799
 Wright A. E., Griffith M. R., Burke B. F., Ekers R. D., 1994, *ApJS*, 91, 111
 Ysard N., Miville-Deschênes M. A., Verstraete L., 2010, *A&A*, 509, L1
 Zonca A., Singer L., Lenz D., Reinecke M., Rosset C., Hivon E., Gorski K., 2019, *J. Open Source Soft.*, 4, 1298

APPENDIX A: TEMPLATE FITTING SPECTRAL INDEX BIASES

There are two biases to consider when using equation (14) to derive spectral indices. The first is associated with the transformation of the template fitted coefficients probability distribution when transformed into a spectral index. We find that this transformation tends to bias the derived spectral index toward *flatter* indices on average (but also has a long tail towards much steeper indices), which becomes significant when the template coefficients have signal-to-noise ratios less than 5. The second bias is associated with the purity of the synchrotron templates used, for C-BASS we must subtract both the free-free component and the background point source population to avoid biasing our spectral index estimates *flatter*. As such, we only use the free-free and source subtracted C-BASS 4.76-GHz data in this analysis. We have quantified these biases using simulations.

When deriving the synchrotron spectral index through template fitting there are two potential forms of bias that must be considered. The first form of bias comes from the transformation of the Gaussian

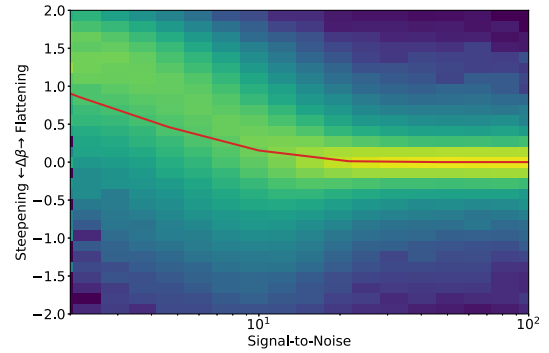


Figure A1. Probability distributions of the change in the measured spectral index for a given template coefficient signal-to-noise ratio. The *red line* indicates the average.

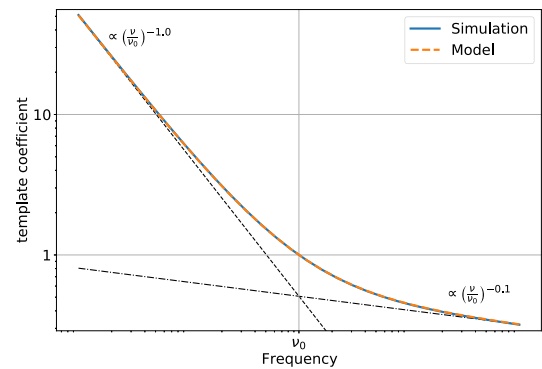


Figure A2. Measured template coefficients when fitting a template that contains two components that correlated with the data set being fitted. The toy model has a steep spectrum component at low frequencies, and a flat spectrum component at high frequencies.

probability distribution associated with the fitted template coefficient (a) into the non-Gaussian probability distribution of the associated synchrotron spectral index through equation (14). In Fig. A1, we show how, for a given signal-to-noise ratio on a synchrotron template coefficient, the associated probability distribution and mean change in the measured spectral index. We find that, on average, as the signal-to-noise ratios approach 10 or less, the average spectral index measured flattens, however, we also find that the probability distribution skews strongly towards much *steeper* spectral indices. This is a well known effect, and attempts to correct for this bias have been implemented in, for example, the COMMANDER analysis (Eriksen et al. 2008). In future analyses, we plan to include a similar correction.

The second form of bias to consider when deriving spectral indices is related to *purity* of the template, i.e. how well does the template represent just a single emission component. In the case of the C-BASS data the map contains a mixture of synchrotron, free-free, and background radio point sources. In the following toy model we will assume we have two components in the template map that are both present in the data map being fitted to. We can define the template as

$$\mathbf{m} = \mathbf{a}_0 + \mathbf{B}_0, \quad (\text{A1})$$

where \mathbf{a}_0 and \mathbf{B}_0 are two uncorrelated brightness distributions. We then fit the template \mathbf{m} to a dataset at a different frequency that can

be described by

$$\mathbf{Z} = \mathbf{a}_0 \left(\frac{\nu}{\nu_0} \right)^\beta + \mathbf{B}_0 \left(\frac{\nu}{\nu_0} \right)^\gamma, \quad (\text{A2})$$

where β and γ are the spectral indices of the two components, and ν_0 is an arbitrary reference frequency. We find that, using the template fitting equations from Section 4, the template coefficient associated with m is

$$\hat{a}_m = \frac{1}{\sigma_{A_0}^2 + \sigma_{B_0}^2} \left[\sigma_{A_0}^2 \left(\frac{\nu}{\nu_0} \right)^\beta + \sigma_{B_0}^2 \left(\frac{\nu}{\nu_0} \right)^\gamma \right], \quad (\text{A3})$$

where we can see the associated template coefficient is the sum of two power laws. Therefore assuming that $\beta < \gamma$, we will expect that at frequencies $\nu \ll \nu_0$ the power law has a spectral index of β and at high frequencies ($\nu \gg \nu_0$) it will follow γ .

A toy model of this effect can be seen in Fig. A2, which compares simulations (solid *blue* line) with the model described by equation (A3) (dashed *orange* line). The plot shows the template coefficient that would be measured between the template frequency

and the data frequency. We can see at high frequencies the flat spectrum component is the dominant contribution and the spectral index that would be measured converges to $\gamma = -0.1$, while at low frequencies it would be dominated by the steep spectrum component, i.e. $\beta = -1$. This model demonstrates the importance of ensuring that the templates used only contain a single emission component otherwise it can severely bias the resulting interpretation of the fitted coefficients.

APPENDIX B: TEMPLATE FITTING COEFFICIENTS AT 22.8GHZ

The coefficients for all regions at 22.8 GHz are given in Tables B1 and B2 for the 4.76-GHz synchrotron template, the τ_{353} dust template, the H α ($f_D = 0.33$) free-free template, and the reduced χ_r^2 value of each template fit. The tables also include the spectral indices derived between the 408 MHz or 4.76 GHz and the 22.8-GHz data. For some regions, no valid spectral index could be derived due to the synchrotron coefficient being negative.

Table B1. Coefficients measured for each region at 22.8 GHz. Coefficients use the C-BASS 4.76-GHz synchrotron template, τ_{353} dust template, and the $f_D = 0.33$ H α template. Synchrotron spectral indices are given for both 4.76-GHz and 408-MHz templates. Each row gives the approximate central Galactic longitude and latitude.

Region	Synchrotron mK/K	Dust K/ τ_{353}	H α μ K/R	χ_r^2	$\beta_{s, 4.76}$	$\beta_{s, 408}$	ℓ ($^\circ$)	b ($^\circ$)
001	8.4 \pm 0.4	9.7 \pm 0.4	4.7 \pm 1.9	1.8	-3.05 \pm 0.03	-2.89 \pm 0.01	130	20
002	5.1 \pm 0.9	11.0 \pm 0.5	-27.5 \pm 6.2	2.7	-3.37 \pm 0.12	-2.96 \pm 0.04	130	30
003	4.7 \pm 1.2	7.8 \pm 0.5	4.8 \pm 4.2	1.4	-3.41 \pm 0.17	-3.13 \pm 0.05	120	40
004	7.6 \pm 0.8	7.0 \pm 0.7	31.6 \pm 3.7	9.2	-3.11 \pm 0.07	-2.91 \pm 0.03	110	20
005	8.1 \pm 1.9	11.0 \pm 0.7	8.6 \pm 1.0	4.7	-3.07 \pm 0.15	-3.15 \pm 0.11	140	20
006	9.9 \pm 0.7	9.0 \pm 1.0	3.6 \pm 2.1	1.5	-2.95 \pm 0.04	-2.94 \pm 0.02	150	30
007	11.8 \pm 1.7	15.7 \pm 0.9	-18.5 \pm 3.8	1.6	-2.83 \pm 0.09	-3.0 \pm 0.03	140	40
008	5.8 \pm 1.1	3.1 \pm 2.2	10.1 \pm 5.1	0.8	-3.29 \pm 0.12	-3.39 \pm 0.16	120	50
009	11.3 \pm 1.4	14.8 \pm 2.1	-4.3 \pm 3.3	1.5	-2.86 \pm 0.08	-3.02 \pm 0.03	100	40
010	9.9 \pm 1.3	8.1 \pm 0.8	18.1 \pm 3.5	6.2	-2.94 \pm 0.08	-2.99 \pm 0.03	100	20
011	5.3 \pm 0.8	10.8 \pm 0.6	12.4 \pm 0.8	5.4	-3.35 \pm 0.1	-3.04 \pm 0.05	130	-10
012	5.1 \pm 1.2	10.9 \pm 0.6	10.8 \pm 1.8	4.1	-3.38 \pm 0.15	-3.1 \pm 0.1	150	10
013	6.2 \pm 1.3	11.8 \pm 0.8	7.5 \pm 4.2	1.6	-3.24 \pm 0.13	-3.14 \pm 0.04	160	20
014	13.6 \pm 0.9	11.9 \pm 0.9	4.0 \pm 5.0	1.0	-2.74 \pm 0.04	-2.97 \pm 0.02	160	40
015	16.0 \pm 2.3	36.3 \pm 4.1	-14.6 \pm 2.8	1.3	-2.64 \pm 0.09	-2.95 \pm 0.02	150	60
016	2.2 \pm 1.0	23.8 \pm 7.0	-27.7 \pm 8.7	1.1	-3.9 \pm 0.3	-3.4 \pm 0.23	120	60
017	9.6 \pm 1.4	5.7 \pm 4.4	-9.2 \pm 4.3	0.8	-2.97 \pm 0.09	-3.07 \pm 0.04	90	50
018	8.7 \pm 1.1	21.0 \pm 1.7	-9.2 \pm 4.8	1.4	-3.03 \pm 0.08	-3.06 \pm 0.03	80	40
019	6.5 \pm 0.4	14.3 \pm 0.9	4.2 \pm 0.5	1.3	-3.22 \pm 0.04	-2.99 \pm 0.02	80	20
020	2.6 \pm 1.3	13.3 \pm 1.1	6.7 \pm 1.1	4.6	-3.79 \pm 0.32	-3.4 \pm 0.32	100	-10
021	7.6 \pm 0.9	12.6 \pm 0.9	8.4 \pm 0.6	1.4	-3.12 \pm 0.08	-2.96 \pm 0.03	120	-20
022	7.3 \pm 0.4	13.7 \pm 0.9	7.2 \pm 0.8	1.6	-3.14 \pm 0.04	-2.96 \pm 0.02	140	-20
023	-7.1 \pm 3.1	10.0 \pm 1.4	15.7 \pm 1.5	77.9	-	-	160	-10
024	1.2 \pm 1.7	9.3 \pm 0.6	16.1 \pm 2.0	15.3	-4.28 \pm 0.9	-	170	10
025	0.8 \pm 1.4	13.1 \pm 0.7	2.5 \pm 2.5	2.9	-4.59 \pm 1.22	-	170	20
026	5.1 \pm 0.8	16.6 \pm 1.7	5.0 \pm 2.0	1.5	-3.36 \pm 0.1	-3.15 \pm 0.03	180	30
027	11.8 \pm 1.4	25.5 \pm 5.3	-9.8 \pm 10.4	2.7	-2.83 \pm 0.08	-2.92 \pm 0.03	180	50
028	9.3 \pm 1.1	24.3 \pm 5.8	4.4 \pm 6.3	1.4	-2.98 \pm 0.08	-3.06 \pm 0.04	170	70
029	7.4 \pm 0.8	24.1 \pm 3.9	-13.0 \pm 5.4	0.7	-3.13 \pm 0.07	-3.28 \pm 0.09	130	70
030	11.5 \pm 1.0	15.5 \pm 4.0	-9.3 \pm 6.0	0.8	-2.85 \pm 0.05	-3.02 \pm 0.03	80	70
031	7.0 \pm 1.0	15.5 \pm 2.6	-8.5 \pm 5.2	0.8	-3.17 \pm 0.09	-3.04 \pm 0.02	70	50
032	10.3 \pm 2.0	12.8 \pm 3.5	-13.8 \pm 6.1	4.9	-2.92 \pm 0.12	-3.33 \pm 0.16	70	30
033	6.3 \pm 0.5	15.0 \pm 0.6	4.5 \pm 1.0	1.4	-3.24 \pm 0.05	-3.12 \pm 0.03	70	20
034	6.5 \pm 1.0	13.4 \pm 0.9	5.1 \pm 0.8	5.7	-3.22 \pm 0.09	-3.0 \pm 0.04	90	-10
035	9.2 \pm 1.2	12.9 \pm 0.7	8.1 \pm 0.7	3.4	-2.99 \pm 0.08	-3.07 \pm 0.06	110	-20
036	6.0 \pm 1.0	14.5 \pm 0.8	-1.9 \pm 4.7	1.0	-3.26 \pm 0.11	-2.99 \pm 0.04	110	-30
037	9.7 \pm 1.1	12.8 \pm 0.8	-2.9 \pm 2.5	1.7	-2.96 \pm 0.08	-3.01 \pm 0.07	130	-30
038	2.6 \pm 1.7	10.3 \pm 1.2	18.7 \pm 3.4	14.7	-3.81 \pm 0.42	-	150	-30
039	17.7 \pm 1.6	5.2 \pm 0.4	2.8 \pm 1.3	30.4	-2.57 \pm 0.06	-2.71 \pm 0.02	170	-10
040	16.2 \pm 4.0	10.6 \pm 0.4	1.2 \pm 1.8	15.4	-2.63 \pm 0.16	-2.93 \pm 0.09	180	10
041	6.6 \pm 0.8	8.6 \pm 1.2	4.7 \pm 1.6	1.3	-3.21 \pm 0.08	-3.09 \pm 0.04	190	20
042	3.5 \pm 2.0	12.9 \pm 2.1	10.5 \pm 5.0	1.7	-3.61 \pm 0.37	-3.49 \pm 0.3	200	40
043	6.0 \pm 1.0	15.9 \pm 2.6	-1.1 \pm 5.1	1.0	-3.27 \pm 0.11	-3.07 \pm 0.05	200	60
044	7.4 \pm 1.5	31.8 \pm 5.9	-7.7 \pm 7.5	1.2	-3.13 \pm 0.13	-3.24 \pm 0.09	200	80
045	4.5 \pm 1.1	43.5 \pm 7.7	-12.6 \pm 13.6	2.0	-3.45 \pm 0.15	-3.23 \pm 0.09	50	80
046	9.8 \pm 0.4	19.5 \pm 1.3	-18.0 \pm 4.5	0.7	-2.95 \pm 0.03	-3.02 \pm 0.01	50	60
047	8.2 \pm 1.1	19.3 \pm 1.8	1.8 \pm 5.1	3.0	-3.07 \pm 0.09	-3.15 \pm 0.04	50	40
048	6.6 \pm 0.6	15.7 \pm 0.8	-0.2 \pm 1.2	1.7	-3.21 \pm 0.06	-3.07 \pm 0.02	60	20
049	7.1 \pm 0.6	11.1 \pm 0.5	9.7 \pm 0.5	3.2	-3.16 \pm 0.05	-2.99 \pm 0.03	60	10
050	5.6 \pm 1.4	7.9 \pm 0.7	7.7 \pm 0.7	3.7	-3.31 \pm 0.16	-3.43 \pm 0.19	70	-10
051	5.8 \pm 0.7	15.7 \pm 1.9	6.6 \pm 0.5	2.3	-3.29 \pm 0.08	-3.09 \pm 0.04	90	-20
052	3.9 \pm 1.3	14.3 \pm 0.9	0.4 \pm 5.1	1.3	-3.54 \pm 0.22	-3.07 \pm 0.07	120	-40
053	8.9 \pm 0.9	12.0 \pm 0.9	-0.3 \pm 4.6	2.7	-3.02 \pm 0.06	-2.85 \pm 0.02	150	-40
054	14.3 \pm 1.3	14.1 \pm 0.7	5.1 \pm 1.0	13.4	-2.71 \pm 0.06	-2.8 \pm 0.02	170	-30

Table B2. Table B1 continued.

Region	Synchrotron mK/K	Dust K/ τ_{353}	H α μ K/R	χ_r^2	$\beta_{s, 4.76}$	$\beta_{s, 408}$	ℓ ($^\circ$)	b ($^\circ$)
055	-7.6 ± 1.5	11.8 ± 0.8	8.7 ± 1.2	36.8	–	–	180	–10
056	8.9 ± 1.1	9.9 ± 0.4	6.6 ± 0.7	4.8	-3.02 ± 0.08	-2.99 ± 0.05	200	10
057	7.1 ± 0.6	9.3 ± 2.1	5.3 ± 1.3	1.8	-3.16 ± 0.05	-3.04 ± 0.02	200	30
058	9.3 ± 0.8	10.6 ± 1.6	8.3 ± 2.7	0.8	-2.98 ± 0.06	-3.03 ± 0.03	210	50
059	3.8 ± 1.1	10.6 ± 1.5	-0.9 ± 4.3	1.1	-3.57 ± 0.19	-3.12 ± 0.06	230	70
060	8.8 ± 1.2	11.0 ± 1.7	-2.1 ± 13.7	3.0	-3.02 ± 0.09	-3.06 ± 0.04	–70	80
061	8.3 ± 0.3	23.3 ± 2.8	8.6 ± 6.4	1.4	-3.06 ± 0.03	-3.02 ± 0.01	10	70
062	7.0 ± 0.3	15.1 ± 1.5	2.1 ± 4.9	1.3	-3.17 ± 0.03	-3.01 ± 0.01	30	50
063	5.8 ± 0.3	9.2 ± 1.0	28.3 ± 4.2	1.1	-3.28 ± 0.04	-3.07 ± 0.01	40	30
064	6.8 ± 0.9	9.2 ± 0.7	13.5 ± 1.1	5.1	-3.19 ± 0.09	-2.99 ± 0.02	60	–10
065	6.1 ± 0.6	14.3 ± 0.8	5.0 ± 1.1	1.8	-3.25 ± 0.06	-3.22 ± 0.06	70	–20
066	12.9 ± 2.2	14.7 ± 0.7	2.7 ± 8.7	9.3	-2.78 ± 0.11	-2.87 ± 0.05	90	–40
067	8.4 ± 1.0	14.1 ± 0.7	11.0 ± 4.5	2.1	-3.05 ± 0.07	-2.97 ± 0.03	100	–50
068	6.2 ± 0.7	15.8 ± 1.1	-21.7 ± 7.1	1.4	-3.24 ± 0.07	-2.99 ± 0.03	140	–50
069	9.8 ± 1.8	15.6 ± 0.6	1.6 ± 1.3	3.9	-2.95 ± 0.12	-3.3 ± 0.1	170	–40
070	16.0 ± 1.3	13.0 ± 0.8	4.7 ± 0.7	16.5	-2.64 ± 0.05	-2.85 ± 0.03	190	–30
071	6.6 ± 3.3	5.7 ± 1.1	9.9 ± 0.7	82.8	-3.21 ± 0.32	-3.6 ± 1.09	200	–10
072	4.0 ± 0.9	9.0 ± 0.7	11.9 ± 1.1	3.6	-3.52 ± 0.14	-3.12 ± 0.05	210	10
073	5.0 ± 1.2	12.4 ± 1.7	9.0 ± 1.9	1.9	-3.38 ± 0.15	-3.01 ± 0.05	220	30
074	5.6 ± 1.8	8.4 ± 1.9	2.0 ± 3.0	1.8	-3.3 ± 0.21	-3.31 ± 0.12	230	50
075	9.8 ± 3.4	8.5 ± 1.6	-23.2 ± 8.4	8.8	-2.95 ± 0.22	–	270	70
076	7.3 ± 0.6	-2.6 ± 2.2	-5.2 ± 6.6	0.7	-3.14 ± 0.05	-3.13 ± 0.02	330	70
077	6.0 ± 0.4	9.3 ± 2.2	20.0 ± 4.9	1.4	-3.27 ± 0.05	-3.12 ± 0.02	10	60
078	5.2 ± 0.4	12.8 ± 1.3	-0.6 ± 3.9	1.1	-3.36 ± 0.05	-3.17 ± 0.02	20	40
079	5.8 ± 0.4	12.0 ± 0.9	14.0 ± 2.4	1.8	-3.28 ± 0.04	-3.08 ± 0.03	60	–20
080	7.4 ± 0.9	11.4 ± 1.0	14.7 ± 3.3	2.5	-3.13 ± 0.07	-3.1 ± 0.03	70	–40
081	10.2 ± 0.9	13.9 ± 1.5	32.4 ± 9.1	1.8	-2.93 ± 0.05	-3.03 ± 0.04	120	–60
082	7.7 ± 0.9	15.7 ± 1.0	-15.7 ± 4.4	1.0	-3.11 ± 0.07	-3.04 ± 0.03	160	–60
083	8.0 ± 1.3	15.6 ± 0.7	4.5 ± 0.4	7.9	-3.08 ± 0.11	-3.42 ± 0.33	190	–40
084	6.6 ± 2.7	22.0 ± 3.0	5.4 ± 0.8	21.7	-3.2 ± 0.26	-3.04 ± 0.1	200	–20
085	11.2 ± 1.7	7.5 ± 0.5	4.5 ± 0.8	11.3	-2.87 ± 0.1	-3.12 ± 0.13	210	–0
086	5.7 ± 1.0	13.3 ± 1.2	-1.6 ± 1.9	1.5	-3.3 ± 0.11	-3.39 ± 0.16	220	20
087	6.2 ± 1.5	12.7 ± 1.1	4.9 ± 2.7	1.4	-3.25 ± 0.16	–	240	40
088	9.7 ± 2.1	9.2 ± 1.2	7.2 ± 2.4	2.6	-2.96 ± 0.14	-3.05 ± 0.07	260	50
089	8.9 ± 2.3	31.7 ± 22.8	32.0 ± 14.9	47.2	-3.01 ± 0.17	-3.08 ± 0.08	300	60
090	6.9 ± 0.7	11.9 ± 1.0	4.7 ± 1.3	0.9	-3.18 ± 0.06	-3.16 ± 0.04	340	60
091	4.1 ± 1.0	8.6 ± 1.8	56.2 ± 12.7	3.8	-3.51 ± 0.16	-3.15 ± 0.06	10	40
092	5.0 ± 0.4	14.6 ± 0.6	2.5 ± 1.5	2.4	-3.38 ± 0.05	-3.15 ± 0.03	40	–20
093	5.1 ± 0.5	15.7 ± 0.9	4.2 ± 5.2	6.6	-3.37 ± 0.06	-3.08 ± 0.03	60	–40
094	7.6 ± 1.0	14.4 ± 0.9	7.2 ± 3.8	1.1	-3.11 ± 0.08	-3.1 ± 0.04	80	–50
095	7.9 ± 0.8	8.3 ± 2.8	-1.7 ± 8.7	1.8	-3.09 ± 0.06	-3.01 ± 0.03	90	–70
096	3.1 ± 1.1	23.5 ± 1.1	14.3 ± 5.0	1.3	-3.69 ± 0.22	-2.97 ± 0.03	150	–70
097	4.9 ± 0.5	14.6 ± 0.8	5.2 ± 0.3	0.9	-3.4 ± 0.07	-2.95 ± 0.03	190	–50
098	1.3 ± 2.2	22.0 ± 1.4	5.6 ± 0.7	3.6	-4.26 ± 1.13	–	200	–30
099	12.1 ± 1.9	7.0 ± 0.5	4.6 ± 0.4	22.1	-2.82 ± 0.1	-2.94 ± 0.12	220	–10
100	3.4 ± 1.6	7.9 ± 0.4	8.5 ± 0.9	13.0	-3.62 ± 0.29	-3.15 ± 0.11	220	10
101	2.7 ± 1.4	18.2 ± 1.2	8.5 ± 2.3	1.1	-3.78 ± 0.33	-3.19 ± 0.06	240	20
102	7.9 ± 0.7	10.1 ± 1.0	-1.8 ± 2.8	0.7	-3.09 ± 0.06	-3.26 ± 0.12	250	40
103	6.7 ± 0.5	21.7 ± 1.9	-28.5 ± 9.4	1.5	-3.2 ± 0.05	-2.92 ± 0.02	280	50
104	4.7 ± 2.3	31.7 ± 4.0	13.9 ± 3.1	4.3	-3.42 ± 0.31	-3.06 ± 0.1	320	50
105	9.6 ± 1.1	16.9 ± 1.3	-1.1 ± 10.4	4.3	-2.97 ± 0.08	-2.87 ± 0.03	350	40
106	-3.4 ± 2.3	21.5 ± 1.7	12.4 ± 1.5	19.3	–	–	10	30
107	5.5 ± 1.0	12.3 ± 0.8	5.5 ± 3.9	1.5	-3.32 ± 0.11	-3.07 ± 0.04	40	–30
108	6.1 ± 2.6	26.1 ± 6.4	-25.3 ± 14.9	9.8	-3.25 ± 0.28	-3.21 ± 0.12	60	–50

This paper has been typeset from a $\text{\TeX}/\text{\LaTeX}$ file prepared by the author.